Asynchronous glacial dynamics of LGM mountain glaciers in Ikh Bogd massif of Gobi-Altai range, southwestern Mongolia: Aspect control on glacier mass balance

Purevmaa Khandsuren [1], Yeong Bae Seong [1] *, Hyun Hee Rhee [2], Cho-Hee Lee [1], Mehmet Akif Sarikaya[3], Jeong-Sik Oh [4], Khadbaatar Sandag [5], Byung Yong Yu [6]

[1] Department of Geography, Korea University, Seoul 02841, Korea;

[2] Division of Glacial Environment Research, Korea Polar Research Institute, Incheon 21990, Korea;

[3] Istanbul Technical University, Eurasian Institute of Earth Sciences, Sarıyer-Istanbul, 34469, Turkey;

[4] Department of Geography, Kyungpook National University, Daegu 41566, Korea;

[5] Department of Geography, Mongolian National University of Education, Ulaanbaatar 210648, Mongolia;

[6]AMS laboratory, Korea Institute of Science and Technology, Seoul 02792, Korea;

Correspondence to: Yeong Bae Seong (ybseong@korea.ac.kr)

Abstract. Mountain glacier mass balance is affected by factors other than climate, such as topography, slope, and aspect. In mid-latitude high mountain regions, the north-south aspect contrast can cause significant changes in insolation and melt, resulting in local asynchrony in glacial dynamics. This study documents the asynchronous response of two paleoglaciers in southwestern Mongolia to the local topoclimatic factors using ^{10}Be exposure age dating and 2D ice surface modelling. ^{10}Be surface exposure age dating revealed that the Ikh Artsan south-facing valley glacier culminated (M_{IA1}) at 20.1 ± 0.7 ka, coinciding with the gLGM. In contrast, the north-facing Jargalant paleoglacier (M_{J1}) culminated at 17.2 ± 1.5 ka, around Heinrich 1 stadial and during the post-gLGM northern hemisphere warming. Our temperature-index melt model predicts that ablation will be substantially lower on the north-facing slope as it is exposed to less solar radiation and cooler temperatures than on the south-facing slope. Two-dimensional ice surface modeling also revealed that the south-facing Ikh Artsan glacier abruptly retreated from its maximum extent since 20 ka, but the Jargalant glacier on the shaded slope consistently advanced and thickened due to reduced melt till 17 ka. The timings of the modelled glacier culmination are consistent within ±1σ of the ^{10}Be exposure age results. Extremely old ages ranging from 636.2 ka to 35.9 ka were measured for the inner moraines in the Jargalant cirque (M_{J2}-M_{J4}), suggesting a problem with inheritance from boulders eroded from the summit plateau.

Keywords: Glacier, late Quaternary, Mongolia, Ikh Bogd, ^{10}Be surface exposure dating, paleo-erosion surface, uplifted peneplain, 2D ice surface modelling

1. INTRODUCTION

Massive ice sheets or mountain glaciers respond to various climatic forcings that operate on wide geographic scales from local to global. Winter precipitation and summer air temperature are generally considered the most critical factors in controlling glacial mass balance and extent. Understanding the impact of climate on past glacial cycles necessitates a thorough understanding of the timing and amplitude of glacial dynamics. The most recent planet-wide glacial expansion occurred during the global Last Glacial maximum (gLGM) as a result of changes in major climate forcings, e.g., reduced summer insolation, lower tropical sea surface temperatures, and low atmospheric CO_2 content. The remnants of paleoglacial deposits of gLGM are the best preserved among all the ice ages. The gLGM has been extensively studied to ascertain the late Pleistocene changes in ice volume, sea-level fluctuations, feedback on climate, etc. The timing of gLGM has been established using both the marine (e.g., Shackleton, 1967; Shackleton, 2000; Thompson et al., 2003; Skinner and Shackleton, 2005) and terrestrial (e.g., An et al., 1991; Wang et al., 2001; Jouzel et al., 2007; Clark et al., 2009; Fletcher et al., 2010;) paleoclimatic proxies. Based on proxy records, the timing of gLGM is constrained between 26.5 and 19 ka, during which the ice sheets and mountain glaciers reached their maximum and the global sea level was at its minimum (Clark et al., 2009).

The timing and extent of the maximum glaciation in many regions worldwide are poorly understood because distinct ice masses respond differently to local and regional climatic conditions. New geochronological techniques such as in situ cosmogenic surface exposure dating (e.g., Hughes et al., 2013; Heyman, 2014) permit reliable temporal comparisons between the maximum advances of different mountain glaciers.

Evidence from mid-latitude glaciers reveals more complex behavior than that of synchronized 'global' glaciations. In some parts of Asia, for example, the largest glacial extent occurred before Marine Isotope Stage (MIS) 2, >100 ka in the northeastern Tibetan plateau (Heyman et al., 2011a) and late MIS 5/MIS 4 in the Kanas lake, Chinese Altai (Gribenski et al. 2018). In the Tian Shan (Koppes et al., 2008; Li et al., 2014; Blomdin et al., 2016), Altai (Blomdin et al., 2018), Khangai (Rother et al., 2014; Smith et al., 2016; Batbaatar et al., 2018; Pötsch, 2017), and Eastern Sayan, Khovsgol (Gillespie et al., 2008; Batbaatar and Gillespie, 2016) mountains, the largest glaciers dated back to MIS 3, while the MIS 2 glaciers appeared to be smaller (Fig. 1). It is noteworthy that most of the MIS 3 advances are based on a few and/or widely scattered ages of moraine boulders (Blomdin et al., 2016; Gribenski et al., 2018). On the other hand, in the Gichgeniyn range with arid climate conditions, the significant cirque glacier advanced during MIS 1 (Batbaatar et al., 2018). These studies suggest that glaciers in continental interior Asia respond to regional-scale climate fluctuation in different ways; hence, the last glacial maxima differed from place to place. Equilibrium Line Altitude (ELA) depression of MIS 2 maximum varied ~100 to 1100 m from the arid to humid continental environments. ELA depression estimated 800-1100 m in sub-humid regions (Russian Altai, Khangai, Eastern Sayan, SE Tibetan plateau), 500-600 m in semi-arid Gobi Altai mountains, and 100-600 m in the arid northern Tibetan plateau and Tian Shan (Batbaatar, 2018; see the locations in Fig. 1).

In addition to regional climate conditions, non-climatic factors may also control the local extent and dynamics of glaciation. Topographic factors such as catchment morphology, valley width and length, slope, and aspect, can influence glacier dynamics and affect the style of glaciation (Kirkbride and Winkler, 2012; Barr and Lovell, 2014). Glacier mass balance varies with slope aspect, snow avalanche, and wind drifting snow. The north-south aspect contrast in mid-latitude regions with steeper slopes, and higher relief can generate substantial differences in insolation and melt. This difference may be more significant for cirque, small mountain glaciers, or niche glaciers than large valley glaciers or ice caps (Evans and Cox, 2005).

Although spatio-temporal variations in the glacial extent in response to regional climate change have been mentioned in numerous studies, the influence of topoclimatic factors has not been adequately explored. The present study aims to evaluate how topographic shading affects fluctuations in the glacier surface mass balance and consequent changes in glacier thickness and length (advance and retreat) using 2D ice surface model. The spatial and temporal responses of contrastively oriented paleo glaciers to the aspect-driven microclimate are of particular interest to us. We evaluated the response of two mountain glaciers, the south-facing Ikh Artsan glacier and the north facing Jargalant glacier in southwest Mongolia (Jargalant; Fig. 1), to topo-climatic factors. Reliable temporal comparisons between the maximum advances of the two mountain glaciers were made using in situ cosmogenic surface exposure dating (e.g., Heyman, 2014; Hughes et al., 2013). This research will improve our understanding of how mid-latitude glaciers respond to topographic changes.

2. STUDY AREA

2.1 General settings of the study area.

The Gobi-Altai range, a ~800 km long NW-SE trending isolated arc of mountains, is bordered in the northwest by the Mongolian Altai range and separated from the Khangai range by Valley of Lakes (Gobi Lakes Valley). Ikh Bogd massif (Ikh Bogd means 'great saint' or 'great sacred mountain' in Mongolian) is located in the central Gobi-Altai range. Ikh Bogd, Gobi-Altai range is one of the key sites for paleoglaciological, paleoenvironmental research in landlocked arid, semi-arid central Asia.

This massif is over 50 km long, 25 km wide, and rises ~2 km above the surrounding arid piedmont. Terguun Bogd (3957 m asl), the massif's highest peak, is also the highest point in the Gobi-Altai range (Fig. 1b). Ikh Bogd's current stress regime is dominated by a network of thrust faults and sinistral strike-slip faults, that combine to form transpressional pop-up structures (Cunningham et al., 1996; Bayasgalan et al., 1999; Vassallo et al., 2007; Vassallo et al., 2011). The highest part (>3000 m) of the flat summit plateau consists mainly of granite, while lower parts are mostly occupied by gneiss (EIC, 1981; Jolivet et al., 2007; Vassallo et al., 2011).

The flat summit plateau is thought to be a remnant of a formerly extensive Mesozoic erosion surface (Berkey and Morris, 1924; Devyatkin, 1974; Jolivet et al., 2007), surviving most of the Cenozoic due to its rapid and recent uplift after long-term quiescence (Jolivet et al., 2007). Accordingly, erosion in Ikh Bogd is limited to several deep gorges. The summit plateau is well-preserved in unincised areas because of the young age of the massif and arid regional climate (Vassallo et al., 2011).

Headwater systems of intermittent streams merge and turn into main streams, which later flow out of the mountain front and transport abundant sediments into large alluvial fans. Alluvial fans from adjacent valleys coalesce (forming bajadas) and stretch to huge endorheic intermontane basins like the Gobi Lakes Valley (Fig. 2). Numerous prior investigations suggest that the summit plateau of the Ikh Bogd massif lacks Quaternary glacial landforms (e.g., Jolivet et al., 2007; Vasallo et al., 2011). However, some well-preserved moraine ridges have been identified and mapped in some cirques of the neighboring massifs including Ikh Artsan, Jargalant (Batbaatar et al., 2018).

2.2 Climate

Ikh Bogd massif is in the cold Gobi Desert, with high amplitude in diurnal and annual temperatures. The climate of the study area is characterized by a dry, cold winter with limited snowfall and hot summer with more than 65% yearly precipitation coming in summer (Batbaatar et al., 2018). Bayankhongor (Fig. 2), the nearest aimag center to the study area (the largest unit of Mongolian province), is 140 km away and receives 190 mm of precipitation per year (2005-2019 average, NAMHEM, 2020), while it drops to 100 mm (Yu et al., 2017, Fig. 2b, 2c, and 2d) near Orog lake (1168 m a.s.l, Zhang et al., 2022). The closest weather stations to Ikh Bogd are Bayangobi (1540 m a.s.l) in the south and Bogd (1240 m a.s.l) in the north. The long-term mean annual temperature measured as 3.2 ℃ in Bayangobi and 4.4 ℃ in Bogd (Fig. 2c and 2d). The average January temperature was approximately -18 ℃ in both stations (NAMHEM, 2020).

Ikh Bogd experiences long winter, a lower mean annual temperature (-10 °C), and higher precipitation (200 mm) than its surrounding regions (Fig. 2a, 2b). Even in summer, the temperature is mostly below 0 ℃ at altitudes above 3800 m a.s.l in Ikh Bogd (Long-term monthly temperatures are calculated using a dry lapse rate of 9.8 ℃/km from nearby Bayangobi weather station; Supplementary 1). It begins to snow in the nearby Gobi Lakes Valley around the end of September, although it melts quickly. Nonetheless, due to the relatively cold temperature, a thin snow cover persists on the summit plateau of Ikh Bogd between the end of September and the middle of April. Occasionally, precipitation in the form of snow occurs during the summer (Landsat imagery, Farr et al., 2007). Compared to the cool summer of Ikh Bogd, surrounding areas have warm summers. The July temperature rises to about 21.8 ℃ in Bayangobi and 23.0 ℃ in Bogd. (Fig. 2d; NAMHEM, 2020).

Strong Siberian high pressure prohibits the entrance of westerlies during winter, while westerlies and southwesterlies are still effective during summer in the study area. The orientation and shape of mobile dunes northwest of Orog lake record the direction of prevailing winds from the northwest (Yu et al., 2019; Mischke et al., 2020; NAMHEM, 2020). Much colder than present-day winters and summers in Mongolia are consistent with the strengthening of the winter high pressure over northern Eurasia. LGM summers were 1 to 7 ℃ colder than today in Mongolia. The southward shift of westerly storm tracks should, therefore, contribute to the lower than present precipitation values (Tarasov et al., 1999). Multi-proxy records indicate that the local LGM climate if the study area was very dry and harsh (Yu et al., 2019).

3. METHODOLOGY

3.1. Field investigation and geomorphologic mapping

We conducted the fieldwork around the Mongolian Altai in July 2018. Prior to fieldwork, we identified glacial erosional and depositional landforms from the ALOS PALSAR DEM with 12.5 m resolution (JAXA/METI, 2007) and oblique imageries of © ArcGIS Earth and © Google Earth. Only two categories of glacial landforms could be identified and mapped from the satellite imageries and DEM analysis, the glacial cirques and hummocky moraines. Glacial cirques, with amphitheater-like glacial erosional landforms, were easily recognized around the highest mountain areas. Identification of hummocky moraine has been made from the previous studies (Batbaatar et al., 2018) and oblique imageries of © ArcGIS Earth and © Google Earth imagery, since the DEM is of insufficient resolution to show the hummocky topography clearly. The mapping was performed in a GIS environment and mapped on 30 m Shuttle Radar Topographic Mission (SRTM), satellite imagery of © Bing Maps and © ArcGIS Earth. Pre-identified moraines were confirmed during fieldwork. They were then categorized based on their stratigraphic position and separation between moraine ridges. The naming of landforms (e.g., valleys) in the research area was based on locality names from a 1:100000-scale topographic map of Mongolia (ALAMGCM, 1970) and a conversation with local herders.

3.2. Equilibrium Line Altitude

Ikh Bogd massif is unglaciated today. Furthermore, the nearest modern glaciers to the study area are in Otgontenger (Khangai) and Sutai (Mongolian Altai), which are approximately 350 to 550 km north and west of the Ikh Bogd massif, respectively. Thus, we could not calculate present ELAs or ELA depression; hence only ELAs for former glaciers (Ikh Artsan and Jargalant paleoglaciers) were estimated.

The THAR method may include a large error when glacier geometry is complex (Benn and Lehmkuhl 2000). Yet, it is more suitable for our study area because it has simple glacier morphology. A relatively lower value of THAR (Meierding 1982) is commonly used in previous studies of mid-latitude glaciers; however, a higher value is applicable according to glacier type or location. We also used a higher THAR ratio of 0.58 because the Ikh Bogd massif must have a higher ratio due to its arid environment during the last glaciation (Gillespie et al. 2008; Felauer et al., 2012; Lehmkuhl et al., 2018).

$$ELA = A_t + 0.58(A_h - A_t) \quad (1)$$

where A_h and A_t are the headwall and toe altitudes, respectively.

A major problem exists in defining the headwall limit of a former glacier, which is very subjective and arbitrary (Porter 2001). The glacial headwall altitude was considered to be 1/3 of the altitude difference between the cirque floor and the top of the rock cliff, which was a similar ratio for schrund-lines estimation in White Mountains, New Hampshire, USA (Goldthwait, 1970). Headwall altitude is extracted from ALOS PALSAR DEM with 12.5 m resolution (JAXA/METI, 2007). The altimetric error (vertical uncertainty) of the DEM is ~5-7 m (Chai et al., 2022, Ferreira and Cabral, 2022). Glacial toe altitude was measured in the field using GPS and confirmed with the altitude from the DEM.

3.3. Cosmogenic ^{10}Be surface exposure dating

We used cosmogenic ^{10}Be surface exposure dating based on the specific sampling procedure described below to determine the timing of the last glacial advances in Ikh Bogd massif (Gosse and Phillips, 2001; Khandsuren et al., 2019). We sampled quartz-rich granitic boulders on the moraine crests, which were not reworked and represented single, distinguishable ice-marginal positions. We sampled boulders that are rooted in the upper flat surface of the moraine crest and away from steep slopes to avoid post-depositional movement such as rolling and sliding downslope. We excluded boulders smaller than 50 cm above ground level that are likely to have been buried, exhumed, or heavily eroded. Samples were obtained by chisel and hammer from the top surfaces of boulders (less than 5 cm thick) to avoid the edging effect. We sampled at least five boulders from each single moraine crest to statistically screen any outliers such as inheritance or post-glaciation reworking.

We followed the laboratory works of Korea University Geochronology Laboratory (Seong et al., 2016), with the revised procedure of Kohl and Nishiizumi (1992). Rock samples were crushed and sieved to obtain a monomineralic quartz and avoid grain size dependency. Meteoric ^{10}Be and other contaminations were removed by successive HF/HNO_3 leaching. Purified quartz grains (250~500 µm) were first spiked with ~1047.8 ppm concentrated ^{9}Be carrier and then dissolved with HF/HNO_3. Fluorides were removed by perchloric ($HClO_4$) acid, while Be was separated from other ions (cations/anions) using ion-exchange chromatography columns. Beryllium hydroxide was recovered using ammonium hydroxides. Consequently, $Be(OH)_2$ gels were dried on high-temperature hotplates. They were calcinated to be oxide forms in a furnace at higher temperatures (800 °C). BeO samples were mixed with Niobium powder to get conductivity and targeted in aluminum target to be loaded into 6 MV tandem Accelerator Mass Spectrometry (AMS) for $^{10}Be/^{9}Be$ ratio measurement in the Korea Institute of Science and Technology. $^{10}Be/^{9}Be$ ratios for each sample were measured relative to the 07KNSTD standard sample 5-1 (Nishiizumi et al., 2007), having a $^{10}Be/^{9}Be$ ratio of $2.71 \times 10^{-11} \pm 4.71 \times 10^{-13}$ (calibrated error). The measured average ^{10}Be to ^{9}Be ratio of the processing blank was $4.53 \times 10^{-15} \pm 1.6 \times 10^{-15}$ (n=2). The exposure ages were calculated using Cronus-Earth online calculator v3 (Balco et al., 2008). ^{10}Be production rate scaling was based on the time-dependent and nuclide-specific LSDn scaling (Lifton et al., 2014). Several studies on the last glacial history in continental central Asia (e.g. Rother et al., 2014, Batbaatar et al., 2018) present ^{10}Be exposure ages referenced to other scaling methods. For a simple comparison, we recalculated their exposure ages with LSDn scaling model. Errors of exposure ages were represented by external uncertainty (1σ confidence level).

We tested the boulder populations to find outliers using the Chauvenet and Pierce criterion and normalized deviation methods (Ross, 2003; Chauvenet, 1960, Batbaatar et al., 2018) before we assigned deglaciation ages of moraine sequences. The idea behind using Chauvenet's criterion is to find a probability band centered on the mean of a normal distribution containing all samples. Any data points that lie outside this probability band can be considered to be outliers. In contrast, Peirce's criterion is based on Gaussian distribution, and the data point is rejected if its deviation from the mean exceeds the maximum allowed deviation (calculated from the standard deviation of the group and Peirce's criterion table). For the normalized deviation, a sample in groups was rejected if its normalized deviation from the group mean (excluding the tested sample) was greater than two (Batbaatar et al., 2018). The sample was excluded from the group if its exposure age was recognized as an outlier in any of these three methods. We also calculated the reduced chi-square value and the relative uncertainty of the group (Balco, 2011) after rejecting outliers. The arithmetic mean and group standard deviation were considered as a representation of the group age. However, we also calculated the total uncertainty, including group standard deviation and external uncertainty (systematic uncertainty) of each sample within the group (Batbaatar et al., 2018). We presented minimum exposure ages assuming zero erosion because it has been negligible (at least for the sampled surface) since the boulders were deposited based on field observations and considering almost negligible erosion in arid regions. We also performed boulder erosion sensitivity tests on our exposure ages, using erosion rates of 1-4 mm kyr^{-1} (Blomdin et al., 2018). We omitted corrections for snow cover and vegetation change due to the ephemeral winter snow cover at the elevations of the sampled boulders (e.g., Gosse and Phillips, 2001) because modern winter snow cover (Oct-Apr) is very thin and no tree cover exists due to aridity.

After rejecting the outliers, Welch's t-test statistics were also used to compare the exposure ages of distal moraines of two groups ($M_{IA}1$ and M_{J1}). Welch's t-test assumes that the sample means being compared for two groups are normally distributed and that the groups have unequal variances. The null hypothesis (H_0) states the means of the two groups are same, while the alternative hypothesis (Ha) states that the means of two groups are unequal. We also performed the t-test with the total uncertainty of the groups instead of group variances at a 0.05 significance level.

Since our study area is considered to be a well-preserved paleo peneplanation surface, the ^{10}Be concentration of the flat summit plateau must be very high. If our sampled boulders have an "inherited" component from the summit plateau, the apparent exposure age should significantly exceed the moraine deposition age. We assumed that the ^{10}Be concentration from extremely old boulders could represent the concentration of the summit plateau itself. Hence, we tried to calculate exposure age and the lowest erosion rate of the summit plateau using the highest measured ^{10}Be concentration from the oldest moraine boulder. Therefore, we selected the highest point (3625 m, 44.6°N, 100.2°E) between the Jargalant and Ikh Artsan cirques that is representable of the summit plateau. The minimum erosion rate was calculated with the "Erosion rate calculator" of Cronus Earth V3.0.2 using elevation and geographical coordinate of the selected point, sampling thickness, and ^{10}Be concentration of the oldest boulder, considering the shielding factor as 1 (unshielded).

3.4. The 2D ice surface modelling

A 2D ice surface model covering 22-16 ka was used to examine the influence of aspect on glacier mass balance and dynamics and to explain the empirical dating results. The model calculates glacier mass balance variation and corresponding vertical changes in the glacial ice surface (3.4.1). Furthermore, it defines the glacier toe location (3.4.2) relative to the changing ELA via ice thickening or thinning. Our simulation cannot model actual glaciers; rather, it examines the possibility that variable melt rates could cause a significant difference in mass balance (Fig. 3).

3.4.1 Glacial surface mass balance model: glacial thinning and thickening.

Glacier mass balance (m) is determined by the summation of net ablation (a, see 3.4.1.1) and accumulation (c, see 3.4.1.2) over a stated period (t):

$$m = a + c = \int_{t_1}^{t_2}(a + c)\,dt \qquad (2)$$

To infer the net gain and loss of glacier mass along the longitudinal profile for both catchments, we calculated and plotted the variations in June, July, August (JJA; see 3.4.1.1) melt and winter precipitation (i.e., snow through the whole year; see 3.4.1.2) during 22-16 ka ago. The elevation of the profile was taken from DEM with 12.5 m spatial resolution in 5 m spatial intervals. Site parameters and input parameters of this model are described in Tables 1 and 2.

3.4.1.1 Glacier ablation: Temperature-index glacier melt model

We assumed that the topography (aspect and slope) is the main factor producing a difference in daily incoming solar radiation on the south- and north-facing slopes. The earth's surface receives more energy as the solar altitude angle (α) is high (zenith angle and angle of incidence are low). The diurnal changes in solar altitude angle are caused by the earth's rotation around its axis, which varies from morning to evening. At sunrise and sunset, the solar altitude angle is 0 degrees, and it reaches its maximum value at noon. Accordingly, in the mountainous area of the northern hemisphere, the south-facing slope receives the highest energy at noon. The north-facing slope, on the other hand, receives little or no energy due to the topographic shading effect (Fig. 2e). Such a diurnal cycle of insolation would result in a major variation in the yearly or long-term mass balance of mountain glaciers (by surface melt) flowing on south- and north-facing slopes on a long-term scale.

Calculating orbital parameters

Combined influence caused by the slow changes in axial tilt (obliquity), shape of the Earth’s orbit (eccentricity), and axial precession results in long-term cyclical changes in daily incoming solar radiation. First, we computed long-term variations in orbital parameters such as obliquity, eccentricity, and longitude of the perihelion (Berger and Loutre, 1991). These main orbital elements cause the long-term variation of solar declination (δ) that produce seasonal variation in solar altitude at the given latitude. Then, the long-term variation of solar declination was used to calculate the hour angle (ω), zenith angle (Z), and angle of incidence (θ) (Eq. 3-11). We calculated all values above related to the orbital parameters in time-dependent manner (Fig. 3).

Calculating hour angle

To define aspect-driven contrast in potential direct solar radiation between south-facing and north-facing valleys, we calculated hourly insolation (Eq. 12) with the same input parameters, except for the topography (aspect and slope; Fig. 3). We calculated cell-by-cell sunrise and sunset hour angles of given topography for each valley (Eqs. 3-9) and gave 15° of increment for every one hour to calculate the hourly insolation, starting from the sunrise hour angle until it exceeds the sunset hour angle.

Sunrise and sunset hour angles on the inclined surface were calculated as a function of latitude, solar declination, slope, and azimuth (Iqbal, 1963). Sunrise hour angle for horizontal surface:

$$\omega_s = \cos^{-1}(-\tan\varphi \tan\delta) \qquad (3)$$

The following equations give the sunrise and sunset hour angles on the surface oriented toward the east.

$$\omega_{sr} = \min\left[\omega_s, \cos^{-1}\left(\frac{-xy-\sqrt{x^2-y^2+1}}{x^2+1}\right)\right] \quad (4)$$

$$\omega_{ss} = -\min\left[\omega_s, \cos^{-1}\left(\frac{-xy+\sqrt{x^2-y^2+1}}{x^2+1}\right)\right] \quad (5)$$

The following equations give the sunrise and sunset hour angles on the surface oriented toward the west.

$$\omega_{sr} = \min\left[\omega_s, \cos^{-1}\left(\frac{-xy+\sqrt{x^2-y^2+1}}{x^2+1}\right)\right] \quad (6)$$

$$\omega_{ss} = -\min\left[w_s, \cos^{-1}\left(\frac{-xy-\sqrt{x^2-y^2+1}}{x^2+1}\right)\right] \quad (7)$$

where x and y are kinds of coefficient to make the equations above simpler (Eq. 1.6.7 of Iqbal, 1983).

$$x = \frac{\cos\varphi}{\sin\gamma\ \tan\beta} + \frac{\sin\beta}{\tan\gamma} \quad (4)$$

$$y = \tan\delta\left(\frac{\sin\varphi}{\sin\gamma\ \tan\beta} - \frac{\cos\varphi}{\tan\gamma}\right) \quad (5)$$

Equations 3-9 are for calculating hour angles in arbitrary surfaces, where ω_s is the sunrise hour angle for horizontal surfaces, ω_{sr}, ω_{ss} is the sunrise and the sunset hour angles on the inclined surface, φ is the latitude, δ is the solar declination angle, β is the slope inclination angle, and γ is the surface azimuth angle.

Calculating zenith angle and angle of incidence

Then, the local zenith angle (Z) and the angle of incidence (θ) were calculated using hour angles at one-hour intervals (ω). The zenith angle is angle between sun rays and normal plane to the surface ($90°-\alpha$) and approximated as a function of latitude, solar declination angle, and hour angle (Iqbal, 1983):

$$Z = \sin\delta\ \sin\varphi + \cos\delta\ \cos\varphi\ \cos\omega \quad (10)$$

and the angle of incidence on the arbitrary oriented surfaces is expressed as:

$$\cos\theta = (\sin\varphi\ \cos\beta - \cos\varphi\ \sin\beta\ \cos\gamma)\ \sin\delta + (\cos\varphi\ \cos\beta + \sin\varphi\ \sin\beta\ \cos\gamma)\ \cos\delta\ \cos\omega + \cos\delta\ \sin\beta\ \sin\gamma\ \sin\omega \quad (11)$$

where β is the slope inclination angle and γ is the surface azimuth angle.

Calculating daily insolation and daily melt

Hourly potential clear-sky direct solar radiation (I) was calculated as (Hock, 1999):

$$I = I_0 \left(\frac{R_m}{R}\right)^2 \Psi_a^{\left(\frac{P}{P_0 \cos Z}\right)} \cos\theta \qquad (12)$$

where I_0 is solar constant (1368 W m^{-2};), $(R_m\ R^{-1})^2$ is the eccentricity correction factor of the Earth's orbit for the time considered with R the instantaneous Sun-Earth distance, and R_m is the mean Sun-Earth distance, Ψ_a is the mean atmospheric clear-sky transmissivity (Ψ_a=0.75: (Hock, 1998)), P_h is the atmospheric pressure (NOAA, 1976), P_0 is the mean atmospheric pressure at sea level, Z is the local zenith angle, and θ is the angle of incidence between the normal to the grid slope and the solar beam. Therefore, hourly insolation was summed into daily insolation for corresponding day length (not for 24 hours; Fig. 3).

We calculated daily melt with following equation using daily insolation value (Eq. 12).

$$a = \begin{cases} \left(\frac{1}{n}\mathrm{MF} + a_{ice}\ I\right) T & : \ T > 0 \\ 0 & : \ T \leq 0 \end{cases} \qquad (13)$$

MF is a melt factor (mm d^{-1} $°C^{-1}$), a_{ice} is a radiation coefficient for ice surfaces, I is potential clear-sky direct solar radiation at the ice surface (W m^{-2}), and T is the time-dependent monthly mean temperature (°C). Furthermore, we integrated (summed) the daily melt into monthly and summer melt, which is the same with the total ablation in this model (Fig. 3).

Calculating time-dependent temperature.

We calculated the time-dependent temperature of the study area in the following order:

1) Present-day monthly air temperatures (T) for both cirque headwall altitudes (3533.3 m in Jargalant, 3508.3 m in Ikh Artsan) were calculated from the two nearest national weather stations using a summer adiabatic lapse rate of 8 °C km^{-1} (Batbaatar et al., 2018). Bayangobi weather station (1540 m a.s.l.) is 27 km SE of the study region, and Bogd (Horiult) weather station (1240 m a.s.l.) is 45 km NW (Fig. 2c).

2) We use only summer temperature because even today, monthly mean temperatures between August to May are less than 0 °C, in which no melt occurs (NAMHEM, 2020). The long-term average of the extreme minimum temperature at the mean glacial toe altitude (Ikh Artsan and Jargalant) is -5.2 °C (calculated from Bayankhongor 1874 m) a.s.l using a lapse rate of 8 °C/km). The JJA mean temperature at the cirque headwall altitude was measured as 5.4 °C in the Ikh Artsan valley and 3.5 °C in the Jargalant valley. We chose the value of 5.4 °C for the summer temperature of the study area and used further calculations (see supplementary 1 file).

3) We obtained a time-dependent summer temperature since 22 ka. LGM summer temperature was easily calculated by subtracting known LGM summer temperature anomaly (1–7 °C by Tarasov et al., 1999) from the present-day temperature of the study area. The modern and LGM summer temperature of the study area (5.4 °C) was calibrated to Greenland temperature data from the NGRIP ice core (Buizert et al., 2018) since 22 ka to obtain time-dependent temperature variation (see supplementary 2 file).

4) LGM summer temperature anomalies ranging from -5.0 °C to -6 °C were applied to calculate glacial melt since 22 ka (see supplementary 2 file).

3.4.1.2 Glacier accumulation and snow data

Climatologies at high resolution for the Earth's land surface areas (CHELSA) provides a high resolution, downscaled centennial climate model data since 20 ka. We used CHELSA-TraCE21k 1 km monthly precipitation time series (Karger et al., 2017). Precipitation data between 22–20 ka was considered the same as 20 ka data. Only snowfall at the mean altitude of each valley was considered glacial accumulation, which occurs when the monthly average temperature is below 0 ℃.

3.4.2 Glacial advance and retreat model based on glacier thickness change

Finally, a simple 2D ice surface model reconstructed paleoglacier behavior for 22–16 ka in the study area. First, we created small initial glacial surface profiles on both valleys using the 2D ice surface model developed by Benn and Hulton (2010). We computed the ice surface elevation (ice thickness) along the profiles in both valleys with this model. The model requires (1) assumed yield stress describing a glacier's basal shear stress and (2) a shape factor accounting for the valley-drag effects. We plot the ice profile with 5 m spacing along the mid-line of each valley (Fig. 8d, e), assuming constant basal shear stress of 50, 100, 150, 200, and 300 kPa. Shape factors were calculated perpendicular to the profile with the same spacing with the profile. Subsequently, we calculated the glacier mass balance for 22–16 ka using our temperature-index melt model results and paleo snow accumulation data. Therefore, we applied corresponding paleo mass balance values on the initial ice thickness profiles. Ikh Artsan and Jargalant glaciers are mostly developed within a cirque. The maximum erosion related to the rotational movement beneath a cirque is closely linked to the ELA for cirque glaciers (Dahl et al., 2003). Hence, in our model, the thickest ice surface related to the maximum erosion was considered as ELA. Accordingly, variations in paleo ELAs were calculated regarding the ice thickness change. Eventually, we used the simple quadratic function formula ($f(x)=ax^2 + bx + c$) to determine the location of the glacial toe based on ELA and headwall altitude values (Benn and Hulton, 2010). With the glacial toe location, we could evaluate the paleoglacier advance and retreat at any time of interest.

4. RESULTS

4.1 Field observation and moraine stratigraphy

In Ikh Bogd, late Quaternary glaciation is almost confined within the cirque, extensive valley glacier networks were absent. Glaciers in Ikh Artsan and Jargalant valleys were also restricted in the cirques and flowed shortly down to elevations of ~3000 m a.s.l. Jargalant valley merges to the largest valley on the northern flank called Bituut river valley (Fig. 1b). This large drainage only experienced glaciations in the form of short cirque-valley glaciers, like in Jargalant valley. The massif was limited to small single (no networking) cirque-valley glaciers is best explained by the arid climate of the interior of the Gobi Desert.

Ikh Artsan cirque is smaller and its glacial valley is shorter (~1 km) than Jargalant. The best-preserved moraines, with at least seven to eight morainal crests, occur in the Ikh Artsan cirque (Fig. 4; Fig. 6a; Batbaatar et al., 2018). The farthest moraine sequence (M_{IA1}) was distinguished by down-valley stratigraphic position and long flat ridge along the valley side (Fig. 4a). M_{IA1} moraine is composed of thick, unsorted glacial debris of different particle sizes (from silt to boulder) with huge granitic boulders at the top. Towards the left, the moraine is cut by an intermittent stream, forming a deep valley (Fig. 4).

The Jargalant paleoglacier has a larger accumulation area and length than Ikh Artsan glacier, advancing 1.5 km downvalley. The moraine stratigraphy of Jargalant hummocky moraine was quite complicated. The original moraine surface of the inner moraines has been dissected by longitudinal stream forming the parallel moraine mounds or elongated moraine ridges along the valley. In the field, we matched such uneroded surfaces (or ridges) with the similar elevation and assumed them as an individual sequence. Stratigraphically, we identified four different moraine sequences in the Jargalant complex (M_{J4}, M_{J3}, M_{J2}, and M_{J1}, from youngest to oldest; Figs. 5 and 6). M_{J4}, M_{J3}, and M_{J2} moraines are distinctively separated on the left side of the valley. Elongated moraine feature (M_{J3}, M_{J2}) at the right side of the valley looks like a single flow feature. However, we assumed that the original form of the moraine (separation) had been removed or reworked by the stream erosion (Fig. 6c). According to these matters, some moraine boundaries are still uncertain, hence we marked the boundary with dashed line (Fig. 5 and Fig. 6b, c). M_{J4} moraine lies between 3365–3410 m a.s.l, containing angular to sub-angular clast-supported pebble to boulders. Downvalley from the M_{J4} moraine, M_{J3} and M_{J2} moraines have been longitudinally dissected by stream channels and uneroded moraine surface forms elongated parallel moraine ridges with smooth matrix-supported flat tops and steep clast-supported sides. These streams are filled with the till and angular water-lain sediments. The oldest moraine (M_{J1}) was deposited further downvalley, consisting of a single moraine ridge with large granitic boulders lying on the finer matrix-supported deposit. We mapped the extent of the most distal moraine ridge from the lower end of M_{J2} moraine to the point where the slope changes abruptly. We speculate that this oldest moraine may have extended far enough to reach the Bituut valley; however, beyond this point, the moraine would have been reworked by post glacial processes and lateral erosion of Bituut river (Fig. 5 and Fig. 6b, c).

4.2. Late Pleistocene ELA reconstruction

LGM ELA was calculated for M_{IA1} and M_{J1} moraines (Table 3). We estimated the former ELA using a headwall altitude of 3508–3532 m. The terminal moraine was also identified at an elevation of 3222 m a.s.l in the Ikh Artsan valley. Accordingly, the ELA for the M_{IA1} moraine was 3388 m a.s.l. In contrast, a large terminal moraine was deposited at 2998 m a.s.l in Jargalant valley. The ELA associated with M_{J1} moraine was 3308 m a.s.l., about 80 m lower than M_{IA1} moraine.

4.3. ^{10}Be surface exposure age dating

We present 28 new ^{10}Be exposure ages obtained from the boulders associated with five different moraine sequences, M_{IA1} in Ikh Artsan valley and M_{J1}, M_{J2}, $M_{J3,}$ and M_{J4} in Jargalant (Table 4; Fig. 6).

Ikh Artsan valley: seven granitic boulders (IAM001 to 007) sampled from the most distal moraine ridge ranged in age between 21.2 ± 1.5 to 19.1 ± 1.3 ka. ^{10}Be exposure ages from this moraine sequence were well-clustered, and none of the three methods (Chauvenet, Pierce, and standardized deviation) detected outliers. The moraine formation age was found to be 20.1 ± 0.7 ka (20.1 ± 1.6 ka with total uncertainty), $R\chi^2$ was 0.29, and group relative uncertainty was calculated as 4% (Fig. 7).

Jargalant valley: twenty-one granitic moraine boulders on the four moraine sequences were targeted. Five to seven boulders from each moraine crest were sampled. Outliers were detected and rejected by Pierce and normalized deviation criteria. Because, the results from Pierce and normalized deviation methods were consistent, however, Chauvenet method could not recognize some outliers which were recognized by Pierce and normalized deviation criterions. Exposure ages from the innermost M_{J4} moraine ranged from 636.2 ± 45.1 to 177.3 ± 11.3 ka. The oldest age (JAM003, 636.2 ± 45.1 ka) was excluded, and the four remaining ^{10}Be exposure ages provided a mean age of 212.9 ± 45.9 ka (212.9 ± 47.9 ka with total uncertainty). Five boulders from the M_{J3} moraine ranged in age between 209.0 ± 26.1 to 35.9 ± 8.0 ka. The group mean age was calculated as 69.9 ± 39.4 ka (69.9 ± 41.5 ka with total uncertainty) after rejecting an outlier of 209.0 ± 26.1 ka (JAM008). Boulders from the M_{J2} moraine yielded ages from 284.9 ± 18.4 to 162.1 ± 10.2 ka with a mean exposure age of 193.7 ± 36.7 ka (193.7 ± 41.1 ka with total uncertainty) after rejecting the oldest age of 284.9 ± 18.4 ka (JAM012). Samples from the distal moraine of Jargalant valley (M_{J1}) ranged in age from 18.9 ± 1.7 to 10.6 ± 0.8 ka. The arithmetic mean age for this moraine sequence was 17.2 ± 1.5 ka (17.2 ± 2.1 ka with total uncertainty) without the youngest age of 10.8 ± 0.5 ka (JAM016). The group was relatively well clustered, and its relative uncertainty was 9% and $R\chi^2$ = 1.18 (Fig. 7). For erosion rates of 1-4 mm kyr^{-1}, an exposure age of 10 ka calculated assuming zero erosion would underestimate the true age by 1-4% and an age of 20 ka by 2-7%. Samples with longer exposures (boulders with inheritance) older than 100 ka, were increasingly sensitive to erosion; i.e., JAM10 (123.8 ka) had an impact, increasing ages with 12-125% for 1-4 mm kyr^{-1} and JAM03 (636.2 ka) was saturated even for 1 mm kyr^{-1} boulder erosion rate.

Our age dating results from most distal moraines of Ikh Artsan (20.1 ± 1.6 ka) and Jargalant (17.2 ± 2.1) coincide within the narrow range (19.2-18.5 ka) as we apply total uncertainties to the group mean. However, T-test reveals (T=3.928, P=0.001) that the exposure ages from the distal moraine of Ikh Artsan presented a statistically significant difference from that of the Jargalant based on standard deviations (variance) of the two groups. Likewise, the exposure ages of the two groups were different in 0.05 significance level (T=2.665, P=0.044) using total uncertainties instead of the variance.

Boulders from inner moraines (M_{J4}, M_{J3}, and M_{J2}) presented older (~636.2–35.9 ka) exposure than the timing of the maximum extent unlike morphostratigraphy-the inner moraines should be younger than the distal moraine (M_{J1}). The unexpected, significant inheritance has been widely recognized around the globe in the previous studies (Ciner et al., 2017; more references therein), possibly overestimating the real deposition age of moraine. We interpret that the unexpected older exposure ages (~636.2–35.9 ka) from M_{J4}, M_{J3}, and M_{J2} moraines of Jargalant valley strongly imply the inheritance from the summit plateau. These unusually old boulders are pieces of the summit plateau that were transported onto the glacier surface by rockfall, which seems to happen in recent times as well. For temperate glacier, rock fracturing occurs not only on the headwall above the glacier, but also within the bergschrund (bottom of the headwall) by ice segregation. This kind of undermining (sapping) process or/and glacial debutressing would drive consequent upper headwall collapse and give a large amount of rock supply to the glacier (Sanders et al., 2012; Table 4; Fig. 6b). ^{10}Be concentration of the oldest sample (JAM003 with ^{10}Be concentration of ~262.9×10^5) likely represents nuclide concentration at the surface of the summit plateau. The production rate for the summit plateau (60.49 atoms g^{-1} yr^{-1}) must be higher than the moraine samples (38.45 atoms g^{-1} yr^{-1}) due to its higher elevation (3625 m) than sampling sites and 100% exposure (topographic shielding is 1) to cosmic-ray bombardment. With a high ^{10}Be concentration of JAM003 and production rate of summit plateau (3625 m a.s.l), the assuming exposure age of the flat summit plateau was calculated as 442.3 ± 29.8 ka, and the corresponding erosion rate was calculated as 1.23 ± 0.10 mm kyr^{-1}.

4.4. Results from 2D ice surface modelling

We ran the potential direct solar radiation model applying to a 12.5 m resolution DEM for a more realistic comparison. The model suggests that the aspect largely affects the incoming potential clear-sky solar radiation. The result approved that the south-facing slopes in mountainous regions receive more solar radiation than the north-facing slope in our study area. At solar noon, the sun is always directly south in the northern hemisphere; hence southern slopes of the mountainous area receive their maximum insolation. However, the orientations of the two valleys are not true north or south. The azimuth of the Ikh Artsan is 247° (SSW), and for the Jargalant it is 40° (NNE). According to the exact orientation, the peak of the daily insolation contrast between two valleys is calculated between 3 to 4 pm, not at noon. The current June solstice incoming daily solar radiation in Ikh Artsan valley was 8527.34 WH m-2 and 7714.35 WH m-2 in Jargalant valley, whereas solar radiation was lower during 22 ka, 8460.07 WH m-2 in Ikh Artsan and 7604.54 WH m-2 in Jargalant. Although both valleys received maximum insolation in the first to the middle half of June, the maximum difference in incoming daily solar radiation occurred at the end of August. The main difference in the daily incoming solar radiation ranges from 10–24% on summer days over the period of 22-16 ka. The spatial distribution of potential direct solar radiation of the study area is given in Fig. 8. Typically, the total daily insolation anomaly of summer solstice in 20 ka from present-day and integrated total daily insolation for 22-16 ka were described on the 12.5 m grid cells (Fig. 8d, e). In the same way, 14% excess of total summer insolation was observed on the southern slope during the modelling time interval of 22–16 ka (Fig. 8f; see supplementary 2 file).

For simplicity, the melt was calculated (Eq. 12) along specific profiles of Ikh Artsan and Jargalant valleys (Fig. 8e, f). In accordance with the incoming solar radiation contrast, melt rates on south-facing slopes exceed those on north-facing slopes, as would be expected. If modern glaciers existed in Ikh Bogd, the present-day summer melt would be calculated as 4.0 m in Ikh Artsan valley and 3.7 m in Jargalant, respectively. This was a substantially high melt rate in the arid, cool climate of the study area. The temperature-index melt model discovered that 5% of melt excess in June solstice of any year between 22–16 ka was observed on the south-facing slope. Approximately 8% of the difference in summer melt in any year was observed for 22–16 ka (Fig. 8f, see supplementary 2 file)

We run our 2D ice surface model for many times using different values of basal shear stress, LGM summer temperature anomalies, and site temperature (Supplementary material 2). The cirque and valley dimensions reflect the glacier size (including thickness), and the intensity of former glacial erosion (Barr and Spagnolo, 2015). The normal stress acting on the glacier bed is mainly a result of the weight (thickness) of a glacier. Jargalant glacier is 2.7 times larger in area than Ikh Artsan and twice as long in glacier length, forming a large, deep, and well-developed cirque. According to the glacial valley size, we chose the higher basal shear stress for Jargalant valley (200 kPa) and the smaller value for Ikh Artsan valley (100 kPa). LGM summer temperature anomalies ranging from -6 ℃ to -5 ℃ with 0.1 ℃ intervals were applied the same for both glaciers. Some previous studies suggest that temperature is lower on the north-facing slopes at the same altitude. On the north-facing slope of Taibai, Qinling mountains, JJA monthly mean temperature is measured 0.5–1 ℃ lower than on the south-facing slope in the altitude range of 1250–3750 m (Tang and Fang, 2006). Therefore, we applied two different temperature values for north-facing Jargalant glacier; 1) using the same present-day temperature with Ikh Artsan valley; and 2) using the lower present-day temperature for Jargalant valley than Ikh Artsan.

Case 1. Applying the same present-day temperature: When we use the same present-day temperature and the same LGM anomaly of -5.5 ℃, the modelled chronology of the maximum extents (20.2 ka) of two glaciers were similar and consistent with the Ikh Artsan terminal moraine age dating result (20.1 ka). According to this model (case), Jargalant moraine advanced maximally 20.1 ka and probably reached to Bituut valley.

Case 2. Applying the different present-day temperatures: For the Jargalant glacier, we applied lower present-day temperature by -1 ℃ to -0 ℃ (at 0.1 ℃ interval) than Ikh Artsan. The run yielded different chronologies of maximum ice expansions. Only a small temperature change between the south- and north-facing slope forced two glaciers to behave asynchronously, the north-facing glacier got have 2.70–3.46 kyr of lag in the timing of the maximum extent. When we applied -5.5 ℃ of LGM summer temperature anomaly and present-day summer temperature in Jargalant 0.5 ℃ lower than in Ikh Artsan, Ikh Artsan glacier reached its maximum extent near 20.2 ka. In contrast, the Jargalant glacier maximally advanced approximately at 17.1 ka. This result perfectly fits our ^{10}Be moraine age dating results (20.1 ka and 17.2 ka).

5. DISCUSSION

5.1. Asynchronous glaciation in mid-latitude ranges

Recent glacial chronologies from mid-latitude mountain ranges in North Atlantic region document that Laurentide, Scandinavian ice sheets and number of valley glaciers behaved synchronously, advancing to their maximum extent at roughly the same time as the gLGM (26.5–19 ka). However, some experienced pre-LGM glacial maxima, while others stagnated, re-advanced, continuously advanced even farther during the subsequent Heinrich Stadial 1 (HS-1, 17.5-14.5 ka), displaying both inter-range and intra-range asynchrony (Laabs et al., 2009; Young et al., 2011; Licciardi and Pierce 2018; Palacio et al., 2020).

In Europe, large-scale inter-range asynchrony (several tens of kyr) of last glacial termination was common. Cosmogenic surface dating from the Alps and Turkey provides nearly synchronous last glacial maxima with the gLGM (26.5–19 ka, MIS 2). Whereas other numerical dating techniques, including radiocarbon, U-series, and OSL, indicate earlier local glacial maxima (80–30 ka, MIS 4 to MIS 3) in the Cantabrian Mountains, Pyrenees, Italian Apennines and Pindus Mountains (e.g., Jimenez-Sanchez et al., 2013; Oliva et al., 2019). Another inter-range asynchrony was observed in mountain glaciers of North America. They reached their maximum extent from as old as 25–24 ka for some moraines and outwash in the Sierra Nevada to as young as 17–15 ka for some terminal moraines in the Rocky Mountains but a clear central tendency exists with a mean of ~19.5 ka (Young et al., 2011; Laabs et al., 2020; Palacios et al., 2020). Relatively younger ages (HS-1) across the mountains located in the higher latitude were interpreted as a sign of glacial post-LGM culmination in response to increased delivery of westerly derived moisture which reached the northern continental interior of the western U.S after the large ice sheets started to retreat (Licciardi et al., 2001; Licciardi et al., 2004; Thackray, 2008). For instance, younger exposure ages of the last glacial maxima in the western Uinta mountains, compared to mountain ranges farther east and north, reflected the influence of pluvial Lake Bonneville after the recession of the Laurentide ice sheet to the north (Laabs et al., 2009).

Medium scale inter-range asynchrony (several thousand years) was observed in the Yellowstone plateau. Terminal moraines dated to ~17 ka are common in valleys along the northeastern mountains (e.g., Eightmile, Chico, Pine Creek, S.Fork Deep Creek, Cascade Canyon, and Gallatin) of the Great Yellowstone plateau. Glaciers in the Teton Range (southwestern part of the plateau) have terminal moraine with the age of ~15 ka. Local LGM maxima dated to ~19.8 to 18.2 ka in the western part of the plateau (Beartooth Uplift). Licciardi and Pierce (2018) suggested that shifting orographic precipitation patterns due to the formation of ice dome and change in ice flow direction caused asynchrony in the Great Yellowstone region.

Very few glacial chronologies, if any at all, record intra-range asynchrony during the most recent glacial termination. Age dating results from some relatively well-studied mountain ranges (Wasatch, Uinta, Bighorn ranges in North America) present intra-range asynchrony in glacial maxima in their various aspect (Laabs et al., 2020). Some of them had LGM ages ranging from hundreds to thousands of years from valley to valley. In the Wasatch range, terminal moraines dated to ~21.9 ka (Laabs and Munroe, 2016), ~20.8 ka, 17.3 ka (Laabs et al., 2011) in three western valleys, 19.6 ka in the southwestern valley and 17.6 ka and 17.3 ka in the southeastern valleys (Quirk et al., 2020). Similarly, the last glacial terminal moraine age difference of ~1 kyr was observed between the north-facing and south-facing slope, Eastern Pyrenees (Delmas et al., 2011; Delmas et al., 2008). Even glaciers on the same oriented slope contain some chronology difference. LGM moraine chronology from the three valleys on the east side of the central Sawatch range varies from 22.3 ka to 19.9 ka (Young et al., 2011).

Nevertheless, we suggest that some internal, external, analytical uncertainties associated with sampling, measurements, or/and statistical approach can cause the low magnitude of asynchrony in such small intra-range or massif. Some studies have attributed intra-range asynchrony in terminal moraine ages to contrasting valley glacier response times related to topography, ice dynamics and/or differences in glacier shape and hypsometry (Young et al., 2011, Licciardi and Pierce, 2018). As mentioned above, large and medium-scale asynchrony in the mountain glaciers across the North Atlantic region is mostly explained by precipitation distribution due to the relative location of the moisture source area and atmospheric circulation contributed by topography. However, the intra-range or intra-massif scale of asynchrony in the last glacial period needs further research to understand fully.

5.2. Inter-range asynchrony in ice expansion of last glacial cycle across the western Mongolia

Some ^{10}Be exposure ages of the glacial erratic from the mountain ranges nearby Ikh Bogd show the significant glacial advances between LGM to the Holocene (Fig. 9). The largest ice extent was dated as ~22.0 ka on the western flank of the Sutai (Batbaatar et al., 2018). On the other hand, the farthest ice expansion corresponds to MIS 3 in the Khangai mountain range (Rother et al., 2014; Smith et al., 2016; Pötsch, 2017; Batbaatar et al., 2018). In the Gichgeniyn mountains, Holocene (8–7 ka) glaciers advanced with a similar magnitude to their local LGM position. Generally, two main glacial stages, LGM and post LGM (~17–16 ka), were observed within MIS 2 in Mongolia (Rother et al., 2014; Batbaatar and Gillespie, 2016; Smith et al., 2016; Pötsch, 2017; Batbaatar et al., 2018).

Previous studies using granulometric, palynological, ostracod, and geochemical proxies from the Gobi Lakes Valley reveal occurrence of cold and dry climates during the local LGM (19–18 ka) and Younger Dryas (Felauer et al., 2012; Lee et al., 2013; Yu et al., 2017; Lehmkuhl et al., 2018; Yu et al., 2019; Mischke et al., 2020; Fig. 9). These results are consistent with our exposure ages from two valleys. The warming trend was also present in the Gobi Lakes Valley, where lakes once were desiccated during local LGM, and experienced water level increase after local LGM (e.g., Yu et al., 2017; Mischke et al., 2020).

5.3. Aspect effect on the asynchronous glacial dynamic in Ikh Bogd

Our age dating result reveals that abrupt deglaciation occurred since ~20 ka in the Ikh Artsan glacier. Exposure ages from the M_{JI} moraine (17 ka) should represent one of the following: glacier culmination, survival, or temporary glacial stagnation of the LGM glacier, or glacier re-advance (Fig. 10). In either case, the culmination of the Jargalant glacier near 17 ka implies a major difference in glacier mass balance between south- and north-facing glaciers. Changes in glacier mass balance in small massif or mountain (intra-range) could show large spatial variation due to local topography-induced factors, such as i) snow avalanching, ii) preferential deposition of wind-drifted snow (Florentine et al., 2020), iii) solar radiation and iv) temperature.

i. Periodically occurring snow avalanches support glacial accumulation. Most avalanches have steep slopes between 25° and 50° to slide down (Luckman, 1977). Ikh Artsan and Jargalant valleys are connected to the flat summit plateau and are less steep than the threshold slope of 25°. The average slope was measured as 23° for Jargalant and 18.2° for Ikh Artsan. Very wet snow lubricated with water can cause an avalanche on a slope of only 10 to 25° (Luckman, 1977). However, it is not significantly relevant to our study area because Ikh Bogd and its neighboring area experienced very cold and conditions during MIS 2 (e.g., Yu et al., 2019).

ii. Wind-drifted snow accumulation occurs either with or without snowfall. Wind deflates the snow from the windward slope and redistributes it into the leeward slope. However, the prevailing wind direction of the study area is northwest to southeast, which is almost perpendicular to the orientations of the two valleys. We assume the wind direction during MIS 2 was similar to the present with much strength. Therefore, wind-drifted snow may not significantly affect glacier accumulation. For that reason, we used the same precipitation value in both valleys.

iii. North-facing slopes in the northern hemisphere receive less solar radiation because of the aspect effect. Ikh Bogd locates in a mid-latitude great sunlight climate; furthermore, it has steeper relief which can enhance the aspect effect. (Evans and Cox, 2005). Topographic shading can also influence glacier response and mass balance in mountainous areas (Olson and Rupper, 2019). As expected, our modelling results demonstrate that the north-facing slope receives less summer insolation than the south-facing slope, resulting in reduced glacial melt (5-10%) under the same temperature conditions.

iv. The vegetation, discontinuous permafrost, and modern and paleoglacier distribution and their magnitude in semi-arid mid-latitude regions have contrasting temperatures and soil moisture on sunny and shady slopes (Evans 2006; Barr and Spagnolo, 2015; Klinge et al., 2021). As a result of topographically induced differences of solar radiation and evapotranspiration, forests (consisting of Siberian larch) and discontinuous permafrost are limited to north-facing slopes, whereas mountain steppe covers south-facing slopes in Mongolian forest-step zone (Klinge et al., 2021; Fig. 8b, c). Klinge et al. (2021) determined that the annual incoming solar radiation, permafrost table depth, and soil moisture (topographic wetness index) are significantly correlated. Aspect-driven solar radiation and temperature contrast also give more glacier, lower (altitude) glacier, and larger glacier on the poleward slope (e.g., Evans 2006; Barr and Spagnolo, 2015). For instance, Sutai mountain (closest modern glacier to Ikh Bogd) has large, well-developed valley glaciers that flow northward into low altitude from the ice dome. Still, the glaciers at the south-facing slope end near the summit margin without developing into valley glaciers (Fig. 8c). According to these facts, a small temperature difference is likely to be real and needs to be considered. Our temperature index melt model revealed that applying lower temperature to the north-facing glacier than to the south-facing glacier results in a large melt difference between the two valleys

Among the four topography-aspect induced factors, two are applicable on our study area; incoming solar radiation and temperature difference in south- and north-facing slopes. Our temperature index melt model suggests that an aspect-driven insolation change affects the amount of melt, however in a very small amount. This small reduction in the melt due to the shading effect could not cause a significant difference in glacial mass balance or long-term glacier stagnation or advance. Under the same temperature and different insolation, glaciers on the south- and north-facing slopes across small regions behave almost synchronously. Both Ikh Artsan and Jargalant glaciers culminated near 20.2 ka and abruptly retreated to the cirque headwall. Also, their changes in glacial dynamic were almost the same (See supplementary 2 file). However, no glacier stagnation was observed in the Jargalant valley around 17 ka (i.e., this result does not match our exposure age dating). We sampled from possible most distal moraine from Jargalant valley to avoid sampling from reworked boulders in the steep slope. Likewise, we could not find any other evidence that the Jargalant glacier reached the trunk valley of the Bituut river. If we consider both glaciers moved synchronously, the most distal moraine must locate more downvalley from the ~17 ka culmination. In this case, the geological evidence (terminal moraine) near 20 ka must have been degraded by Bituut mainstream or/and reworked with the mass movement.

When we set the site temperature of Jargalant slightly colder (-0.1 to -1 ℃) than in the Ikh Artsan, glaciers started to behave differently, i.e., they retreat from their distal location asynchronously. When we apply 0.5 ℃ colder temperature to Jargalant than Ikh Artsan, 2D ice surface modelling results are consistent with age dating results. The Ikh Artsan glacier abruptly retreated from its maximum extent near 20.2 ka (age dating result was 20.1 ka). In contrast, the Jargalant glacier advanced almost continuously until 17.8 ka and then began to retreat from its maximum extent by 17.1 ka (age dating result was 17.2 ka) with a brief stagnation around its maximum extent. This result suggests that the exposure age of ~17 ka corresponds to the most extensive glaciation in Jargalant valley. We also assume that the exposure age (17.2 ± 1.5 ka) of the distal moraine (M_{J1}) is the age for maximum extent for the Jargalant valley (Figs. 6b and 6c) because this moraine was not like the small ridge left as a glacier stagnates during its retreat. The M_{J1} moraine was larger than the other moraine sequences, large enough to mark the maximum advance of the glacier.

Based on the age dating and 2D ice surface modelling, we propose that the glaciers on the north- and south-facing slopes of Ikh Bogd may have behaved asynchronously. Glacier volume and area changes are likely to be sensitive to temperature changes in semi-arid and arid regions, such as Ikh Bogd. The glaciers of Ikh Artsan and Jargalant behaved asynchronously due to aspect-induced temperature differences rather than differences in solar insolation.

5.4. Morphostratigraphic mismatch in exposure age dating from erratic boulders, Jargalant valley

5.4.1. Inheritance from the summit plateau

The massif has a steep slope; in particular, the slope reaches 32–70° along cirque walls and incised valleys. Colluvial materials covering hillslopes and long boulder corridors were mainly the results of the active mass wasting process. Particularly, rockfall deposits forming scree and talus apron must be the product of steep slope failure of the summit plateau (Fig. 11). We expected that inner moraine crests would present Holocene or HS-1 exposure in light of morphostratigraphy. M_{J2}, M_{J3}, and M_{J4} moraine crests have exposure ages ranging from 636.2 to 35.9 ka (Table 4, Fig. 6). According to moraine stratigraphy, exposure ages of inner moraines cannot be older than the age of the distal moraine. The apparent ages show antiquity and scatter in its distribution, which cannot be a single geologic event; associating the mean age with the specific timing of glacial termination is not appropriate (Heyman et al., 2011b). It was more likely that the exposure ages from M_{J2}, M_{J3}, and M_{J4} moraines were due to the inherited ^{10}Be concentration produced during prior exposure in the boulders recycled from the cirque wall or paleo summit plateau by rockfall or toppling during glaciation and/or paraglacial period. During termination of the farthest moraine, glacier was long enough to pluck the fresh rocks out along its bed. Also, thick glacier would not allow inherited rocks fall onto the glacier ice (Fig. 12d). After glacier retreat to the cirque, glacier thinning allowed rockfalls with inheritance to the ice surface. Increase of inherited boulders would be contributed by enhanced rock-slope failure (de-buttressing) right after rapid deglaciation (Cossart et al., 2008 ; Ballantyne and Stone, 2012; Hashemi et al., 2022) and ice segregation along the bergschrund. Boulders with inheritance transported to the glacier toe as supraglacier debris. Plucking out by the shortened glacier was not efficient to supply fresh rocks relative to the rock supply with summit plateau inheritance (Fig. 12e).

5.4.2. Cenozoic evolution of the low-lying, high-elevated summit plateau

The flat summit plateau of the Ikh Bogd massif is considered an uplifted paleo-peneplanation surface. The basement structure of Ikh Bogd was formed by the collision of the WNW-ESE to ENE-WSW oriented amalgamated terranes throughout the Precambrian and Paleozoic (Şengör et al., 1993). $^{40}Ar/^{39}Ar$ ages from extrusive volcanic on the Ikh Bogd summit and apatite fission-track data show two significant uplifts that occurred in the Gobi-Altai range and Ikh Bogd history (Jolivet et al., 2007; Vassallo et al., 2007). The first uplift related to early to mid-Jurassic, the region experienced crustal shortening events greater than 2 km. Gobi-Altai has been observed elsewhere in central Asia through this event that is possibly due to a collision between Mongol-Okhotsk and Siberia or the Lhasa and Qiangtang block to the far south in Tibet (Traynor and Sladen, 1995; Dewey et al., 1988; Cunningham, 2010). The present erosional surface of the summit plateau formed just after this Jurassic exhumation and was preserved under a negligible erosion rate. Preservation of this flat summit plateau and its fission-track age indicate quiescence without significant vertical crustal motions continued until the last uplift began (Jolivet et al., 2007; Vassallo et al., 2007; Cunningham, 2010).

The Gobi-Altai range is one of the northernmost far-fields affected by the Cenozoic tectonic collision of India into Asia, which initiated the late Cenozoic reactivation and present-day stress regime (Cunningham et al., 1996; Vassallo et al., 2007). According to the apatite fission track data of Vassallo et al. (2007), the onset of the last and ongoing uplift corresponds to the late Cenozoic, 5 ± 3 Ma. This tectonic reactivation is responsible for creating the high topography (~4000 m a.s.l) seen today, in the response to which faster exhumation is initiated as well (Vassallo et al., 2007).

The paleo-erosion surfaces at high altitudes experienced rapid uplift after a long time of quiescence with low erosion. Cosmogenic nuclides-based denudation rates from global paleo-erosion surfaces in diverse climatic, tectonic, and lithologic environments do not exceed ~20 m Myr^{-1} (Byun et al., 2015). We obtained erosion rate for flat summit plateau using production rate at summit plateau and ^{10}Be concentrations of reworked boulders from M_{J4}, M_{J3}, and M_{J2}

moraines. Calculated bedrock erosion rate for last ~600 ka for summit plateau ranged from 1.23 ± 0.10 mm kyr^{-1} to 25.8 ± 5.75 m Myr^{-1}. The erosion rate of 25.8 ± 5.75 m Myr^{-1} was thought to be a maximum value because erosion probably increases with the increasing elevation of the uplifting massif. This result was harmonious with the long-term (since the last uplift) exhumation rate of 23.6 ± 3 m Ma^{-1} (Vassallo et al., 2011) and Holocene erosion rate of 28 m Myr^{-1} (Jolivet et al., 2007) for the massif. Whereas flatness and the lowest erosion rate of 1.23 ± 0.10 mm Myr^{-1} reveal negligible erosion and notable preservation of paleo-surface for several hundred thousand years. If this erosion rate reflects an average rate that can be applied to the entire flat surface and has been maintained for the total uplift period of the massif (Vassallo et al., 2007), it would account for only the 2 to 7.6 m of erosion.

6. CONCLUSIONS

Central Asian valley glaciers, including Ikh Bogd massif, expanded and shrank, presenting more complex behavior relative to large ice sheets in the northern hemisphere. Regional climate and local non-climatic factors have been playing an essential role in this complexity. Our ^{10}Be dating documents that glacier culmination in Ikh Artsan valley on the southern slope occurred at 20.1 ka (M_{IA1}), generally falling within the gLGM, whereas large terminal moraine formed around 17.2 ka (M_{J1}) in the Jargalant valley on the northern slope.

Asynchrony in glacier expansion has been reported from some of areas in the globe but has not been clearly studied with a combination of geochronologic and numerical modeling approaches. Due to aspect-driven solar insolation change, paleoglacier in the north-facing Jargalant valley melted slower (5-10%) than the glacier in Ikh Artsan valley. However, this amount of melt difference could not produce glacier advance or stagnation for a long period. Asynchronous glaciation was observed across the study area if the LGM summer temperature in Jargalant valley was considered colder than Ikh Artsan and age dating result and modelling result were consistent when we apply 0.5 °C lower temperature to Jargalant to than in Ikh Artsan. According to the lower temperature case, Jargalant glacier retreated from the most extensive position 3000 years later than Ikh Artsan glacier. In the other words, our modelling reveals that the temperature difference driven by aspect on both slopes significantly affects the glaciers to survive longer than when the aspect-driven insolation only affects the glacier melt.

The glacial retreat began soon after the peak of local glacial maximum on both valleys and left several sequences of inner moraines in their heads (cirques). Inner moraine at the south-facing cirque dated to ~ 13.5 ka (Batbaatar et al., 2018), however on the north-facing cirque, transported boulders show a significantly old exposure age (636.2 to 35.9 ka) for inner moraines (M_{J2} - M_{J4}). The summit plateau of the Ikh Bogd massif is one of the oldest known tectonically uplifted surfaces on Earth. It is more likely that extremely old exposure ages are the result of inheritance recycled from rock falls from the paleo-erosional surface of the summit plateau.

Data availability. The data that supports the findings of this study are available within the article [and its supplementary material]

Author contributions. YBS planned the study and proceeded a field investigation with JSO, PK, KS, and CHL. YBS designed a funding acquisition. JSO designed ^{10}Be lab experiments with RHH and BYY. CHL and MKS developed a matlab code of the 2D ice surface modelling and performed the simulation. PK and YBS prepared the manuscript with contributions from all co-authors.

*Competing interests***.** The contact author has declared that neither they nor their co-authors have any competing interests.

Disclaimer. Publisher’s note: Copernicus Publications remains neutral with regard to jurisdictional claims in published maps and institutional affiliations.

Acknowledgments. We thank Dr. Dash for his sincere and productive comments on the earlier version of the manuscript.

REFERENCES

©JAXA/METI., 2007. ALOS PALSAR L1.0 High-resolution terrain corrected dataset. Accessed through ASF DAAC, https://asf.alaska.edu, 25 June 2009. https://doi.org/10.5067/J4JVCFDDPEW1

ALAMGCM.: Topographic map of Mongolia, Geodesy and Cartography division of Agency for Land Administration and Management, Geodesy and Cartography of Mongolia, Ulaanbaatar, Mongolia, 1970.

An, Z., Kukla, G., Porter, S.C., Xiao, J.: Late Quaternary dust flow on the Chinese loess plateau, Catena, 18(2), 125-132, https://doi.org/10.1016/0341-8162(91)90012-M, 1991.

Balco, G: Contributions and unrealized potential contributions of cosmogenic nuclide exposure dating to glacier chronology, 1990–2010. Quat. Sci. Rev. 30, 3–27. https://doi.org/10.1016/j.quascirev.2010.11.003, 2011

Balco, G., Stone, J.O., Lifton, N.A., Dunai, T.J.: A complete and easily accessible means of calculating surface exposure ages or erosion rates from ^{10}Be and ^{26}Al measurements, Quat. Geochronol., 3(3), 174-195, https://doi.org/10.1016/j.quageo.2007.12.001, 2008.

Ballantyne, C.K., Stone, J.O.: Timing and periodicity of paraglacial rock-slope failures in the Scottish Highlands, Geomorphology, 186, 150-161, https://doi.org/10.1016/j.geomorph.2012.12.030, 2013.

Barr, I.D., Lovell, H.: A review of topographic controls on moraine distribution, Geomorphology, 226, 44-64, https://doi.org/10.1016/j.geomorph.2014.07.030, 2014.

Barr, I. D., & Spagnolo, M.: Glacial cirques as palaeoenvironmental indicators: Their potential and limitations. Earth-Sci. Rev, 151, 48-78, https://doi.org/10.1016/j.earscirev.2015.10.004, 2015

Batbaatar, J.: Quaternary Glaciation in Central Asia (Doctoral dissertation), 2018.

Batbaatar, J., Gillespie, A.R.: Outburst floods of the Maly Yenisei. Part II–new age constraints from Darhad basin, Int. Geol. Rev., 58(14), 1753-1779, https://doi.org/10.1080/00206814.2016.1193452, 2016.

Batbaatar, J., Gillespie, A.R., Fink, D., Matmon, A., Fujioka, T.: Asynchronous glaciations in arid continental climate, Quat. Sci. Rev., 182, 1-19, https://doi.org/10.1016/j.quascirev.2017.12.001, 2018.

Bayasgalan, A., Jackson, J., Ritz, J.F., Carretier, S.J.T.: Field examples of strike-slip fault terminations in Mongolia and their tectonic significance. Tectonics, 18(3), 394-411, https://doi.org/10.1029/1999TC900007, 1999.

Benn, D. I., Hulton, N. R.: An ExcelTM spreadsheet program for reconstructing the surface profile of former mountain glaciers and ice caps, Comput. Geosci, v. 36, no. 5, p. 605-610, https://doi.org/10.1016/j.cageo.2009.09.016, 2010,

Benn, D.I., Lehmkuhl, F.: Mass balance and equilibrium-line altitudes of glaciers in high-mountain environments, Quat. Int., 65(Supplement C), 15-29, https://doi.org/10.1016/S1040-6182(99)00034-8, 2000.

Berger, A., Loutre, M.-F.: Insolation values for the climate of the last 10 million years, Quat. Sci. Rev, v. 10, no. 4, p. 297-317, https://doi.org/10.1016/0277-3791(91)90033-Q, 1991,

Berkey, C.P., Morris, F.K.: The peneplanes of Mongolia, Am. Mus. Novit., 136, 1-11, 1924.

Blomdin, R., Stroeven, A.P., Harbor, J.M., Gribenski, N., Caffee, M.W., Heyman, J., Rogozhina, I., Ivanov, M.N., Petrakov, D.A., Walther, M.: Timing and dynamics of glaciation in the Ikh Turgen Mountains, Altai region, High Asia, Quat. Geochronol., 47, 54-71, https://doi.org/10.1016/j.quageo.2018.05.008, 2018.

Blomdin, R., Stroeven, A.P., Harbor, J.M., Lifton, N.A., Heyman, J., Gribenski, N., Petrakov, D.A., Caffee, M.W., Ivanov, M.N., Hättestrand, C., Rogozhina, I., Usubaliev, R.: Evaluating the timing of former glacier expansions in the Tian Shan: A key step towards robust spatial correlations, Quat. Sci. Rev., 153, 78-96, https://doi.org/10.1016/j.quascirev.2016.07.029, 2016.

Buizert, C., Keisling, B., Box, J., He, F., Carlson, A., Sinclair, G., and DeConto, R.: Greenland-wide seasonal temperatures during the last deglaciation, Geophys. Res. Lett., v. 45, no. 4, p. 1905-1914, https://doi.org/10.1002/2017GL075601, 2018.

Byun, J., Heimsath, A.M., Seong, Y.B., Lee, S.Y.: Erosion of a high-altitude, low-relief area on the Korean Peninsula: implications for its development processes and evolution, Earth Surf. Process. Landf., 40(13), 1730-1745, https://doi.org/10.1002/esp.3749, 2015.

Chai, L. T., Wong, C. J., James, D., Loh, H. Y., Liew, J. J. F., Wong, W. V. C., & Phua, M. H.: Vertical accuracy comparison of multi-source Digital Elevation Model (DEM) with Airborne Light Detection and Ranging (LiDAR). In IOP Conference Series: Earth. Environ. Sci., 1053, No. 1, p. 012025, IOP Publishing, 10.1088/1755-1315/1053/1/012025, 2022.

Chauvenet, W.: A Manual of spherical and practical astronomy-Vol. 1: Spherical astronomy; Vol. 2: Theory and use of astronomical instruments. Method of least squares, 5th ed., revised and corr, Dover Publication, New York, 1960

Chen, Y., Li, Y., Wang, Y., Zhang, M., Cui, Z., Yi, C., Liu, G.: Late Quaternary glacial history of the Karlik Range, easternmost Tian Shan, derived from ^{10}Be surface exposure and optically stimulated luminescence datings, Quat. Sci. Rev., 115, 17-27, https://doi.org/10.1016/j.quascirev.2015.02.010, 2015.

Ciner, A., Sarikaya, M. A., Yildirim, C.: Misleading old age on a young landform? The dilemma of cosmogenic inheritance in surface exposure dating: Moraines vs. rock glaciers, Quat. Geochronol., 42, 76-88, https://doi.org/10.1016/j.quageo.2017.07.003, 2017.

Clark, P.U., Dyke, A.S., Shakun, J.D., Carlson, A.E., Clark, J., Wohlfarth, B., Mitrovica, J.X., Hostetler, S.W., McCabe, A.M.: The last glacial maximum, Science, 325(5941), 710-714, https://doi.org/10.1126/science.1172873, 2009.

Cossart, E., Braucher, R., Fort, M., Bourlès, D., Carcaillet, J.: Slope instability in relation to glacial debuttressing in alpine areas (Upper Durance catchment, southeastern France): evidence from field data and 10Be cosmic ray exposure ages, Geomorphology, 95(1-2), 3-26, https://doi.org/10.1016/j.geomorph.2006.12.022, 2008.

Cunningham, D.: Tectonic setting and structural evolution of the Late Cenozoic Gobi-Altai orogen, J. Geol. Soc. London., 338(1), 361-387, https://doi.org/10.1144/SP338.17, 2010.

Cunningham, W.D., Windley, B.F., Dorjnamjaa, D., Badamgarov, J., Saandar, M.: Late Cenozoic transpression in southwestern Mongolia and the Gobi-Altai-Tien Shan connection, Earth Planet. Sci. Lett., 140(1-4), 67-81, https://doi.org/10.1016/0012-821X(96)00048-9, 1996.

Dahl, S. O., Bakke, J., Lie, Ø., & Nesje, A.: Reconstruction of former glacier equilibrium-line altitudes based on proglacial sites: an evaluation of approaches and selection of sites. Quat. Sci. Rev., 22(2-4), 275-287, https://doi.org/10.1016/S0277-3791(02)00135-X, 2003

Delmas, M., Calvet, M., Gunnell, Y., Braucher, R., & Bourlès, D.: Palaeogeography and 10Be exposure-age chronology of Middle and Late Pleistocene glacier systems in the northern Pyrenees: implications for reconstructing regional palaeoclimates, Palaeogeo. Palaeoclimatol. Palaeoecol., 305(1-4), 109-122, https://doi.org/10.1016/j.palaeo.2011.02.025, 2011.

Delmas, M., Gunnell, Y., Braucher, R., Calvet, M., & Bourlès, D.: Exposure age chronology of the last glaciation in the eastern Pyrenees, Quat. Res., 69(2), 231-241, https://doi.org/10.1016/j.yqres.2007.11.004, 2008.

Devyatkin, E.: Structures and formational complexes of the Cenozoic activated stage. Tectonics of the Mongolian People's Republic, Nauka, 41, 182-195, 1974.

Dewey, J.F., Shackleton, R.M., Chengfa, C., Yiyin, S.: The tectonic evolution of the Tibetan Plateau, Philos. Trans. Royal Soc. A., 327(1594), 379-413, https://doi.org/10.1098/rsta.1988.0135, 1988.

EIC.: Geologic map of Mongolia 1:1000000. Environment Information Center of National Agency for Meteorology, Hydrology and Environmental Monitoring, Ulaanbaatar, Mongolia, 1981.

Evans, I. S.: Local aspect asymmetry of mountain glaciation: a global survey of consistency of favoured directions for glacier numbers and altitudes. Geomorphology, 73(1-2), https://doi.org/10.1016/j.geomorph.2005.07.009 166-184, 2006

Evans, I.S., Cox, N.J.: Global variations of local asymmetry in glacier altitude: separation of north–south and east–west components, J. Glaciol., 51(174), 469-482, https://doi.org/10.3189/172756505781829205, 2005.

Felauer, T., Schlütz, F., Murad, W., Mischke, S., Lehmkuhl, F.: Late Quaternary climate and landscape evolution in arid Central Asia: A multiproxy study of lake archive Bayan Tohomin Nuur¢, Gobi desert, southern Mongolia, J. Asian. Earth. Sci., 48, 125-135, https://doi.org/10.1016/j.jseaes.2011.12.002, 2012.

Ferreira, Z. A., & Cabral, P:. A Comparative study about vertical accuracy of four freely available digital elevation models: a case study in the Balsas river watershed, Brazil. ISPRS Int. J. Geo-Inf., 11(2), 106, https://doi.org/10.3390/ijgi11020106, 2022

Fletcher, W.J., Goni, M.F.S., Allen, J.R., Cheddadi, R., Combourieu-Nebout, N., Huntley, B., Lawson, I., Londeix, L., Magri, D., Margari, V.: Millennial-scale variability during the last glacial in vegetation records from Europe, Quat. Sci. Rev., 29(21-22), 2839-2864, https://doi.org/10.1016/j.quascirev.2009.11.015, 2010.

Florentine, C., Harper, J., Fagre, D.: Parsing complex terrain controls on mountain glacier response to climate forcing, Glob. Planet. Change., 191, 103209, https://doi.org/10.1016/j.gloplacha.2020.103209, 2020.

Gillespie, A.R., Burke, R.M., Komatsu, G., Bayasgalan, A.: Late Pleistocene glaciers in Darhad basin, northern Mongolia, Quat. Res., 69(2), 169-187, https://doi.org/10.1016/j.yqres.2008.01.001, 2008.

Goldthwait, R.P.: Mountain glaciers of the Presidential Range in New Hampshire, Arc. Alp. Res., 2(2), 85-102, https://doi.org/10.1080/00040851.1970.12003566, 1970.

Gosse, J.C., Phillips, F.M.: Terrestrial in situ cosmogenic nuclides: theory and application, Quat. Sci. Rev., 20(14), 1475-1560, https://doi.org/10.1016/S0277-3791(00)00171-2, 2001.

Gribenski, N., Jansson, K. N., Preusser, F., Harbor, J. M., Stroeven, A. P., Trauerstein, M., ... & Zhang, W.: Re-evaluation of MIS 3 glaciation using cosmogenic radionuclide and single grain luminescence ages, Kanas Valley, Chinese Altai. J. Quat. Sci., 33(1), 55-67, https: //doi.org/10.1002/jqs.2998, 2018

Hashemi, K., Sarıkaya, M.A., Görüm, T., Wilcken, K.M., Çiner, A., Žebre, M., Stepišnik, U., Yıldırım, C.: The Namaras rock avalanche: Evidence of mid-to-late Holocene paraglacial activity in the Central Taurus Mountains, SW Turkey, Geomorphology, 408, 108261, https://doi.org/10.1016/j.geomorph.2022.108261, 2022.

Heyman, J.: Paleoglaciation of the Tibetan Plateau and surrounding mountains based on exposure ages and ELA depression estimates, Quat. Sci. Rev., 91, 30-41, https://doi.org/10.1016/j.quascirev.2014.03.018, 2014.

Heyman, J., Stroeven, A.P., Caffee, M.W., Hättestrand, C., Harbor, J.M., Li, Y., Alexanderson, H., Zhou, L., Hubbard, A.: Palaeoglaciology of Bayan Har Shan, NE Tibetan Plateau: exposure ages reveal a missing LGM expansion, Quat. Sci. Rev., 30(15-16), 1988-2001, https://doi.org/10.1016/j.quascirev.2011.05.002, 2011a.

Heyman, J., Stroeven, A.P., Harbor, J.M., Caffee, M.W.: Too young or too old: evaluating cosmogenic exposure dating based on an analysis of compiled boulder exposure ages, Earth Planet. Sci. Lett., 302(1-2), 71-80, https://doi.org/10.1016/j.epsl.2010.11.040, 2011b.

Hock, R.: Modelling of glacier melt and discharge: ETH Zurich-, 1999, A distributed temperature-index ice-and snowmelt model including potential direct solar radiation, J. Glaciol., v. 45, no. 149, p. 101-111, https://doi.org/10.3189/S0022143000003087, 1998,

Hock, R.: A distributed temperature-index ice-and snowmelt model including potential direct solar radiation, J. Glaciol., 45(149), 101-111, https://doi.org/10.3189/S0022143000003087, 1999.

Hughes, P.D., Gibbard, P.L., Ehlers, J.: Timing of glaciation during the last glacial cycle: evaluating the concept of a global 'Last Glacial Maximum'(LGM). Earth-Sci. Rev., 125, 171-198, https://doi.org/10.1016/j.earscirev.2013.07.003, 2013.

Iqbal, M.: An Introduction to Solar Radiation, New York, Academic Press, 1983

Jiménez-Sánchez, M., Rodríguez-Rodríguez, L., García-Ruiz, J.M., Domínguez-Cuesta, M.J., Farias, P., Valero-Garcés, B.L., Moreno, A., Valcárcel, M.: A review of glacial geomorphology and chronology in northern Spain: timing and regional variability during the last glacial cycle. Geomorphology 196, 50–64, https://doi.org/10.1016/j.geomorph.2012.06.009, 2013

Jolivet, M., Ritz, J.-F., Vassallo, R., Larroque, C., Braucher, R., Todbileg, M., Chauvet, A., Sue, C., Arnaud, N., De Vicente, R.: Mongolian summits: an uplifted, flat, old but still preserved erosion surface, Geology, 35(10), 871-874, https://doi.org/10.1130/G23758A.1, 2007.

Jones, R., Small, D., Cahill, N., Bentley, M., Whitehouse, P.: iceTEA: tools for plotting and analysing cosmogenic-nuclide surface-exposure data from former ice margins, Quat. Geochronol., 51, 72-86, https://doi.org/10.1016/j.quageo.2019.01.001, 2019.

Jouzel, J., Stievenard, M., Johnsen, S.J., Landais, A., Masson-Delmotte, V., Sveinbjornsdottir, A., Vimeux, F., Von Grafenstein, U., White, J.W.: The GRIP deuterium-excess record, Quat. Sci. Rev., 26(1-2), 1-17, https://doi.org/10.1016/j.quascirev.2006.07.015, 2007.

Karger, D.N., Conrad, O., Böhner, J., Kawohl, T., Kreft, H., Soria-Auza, R.W., Zimmermann, N.E., Linder, H.P., Kessler, M.: Climatologies at high resolution for the earth's land surface areas. Sci. Data., 4, 170122, https://doi.org/10.1038/sdata.2017.122, 2017.

Khandsuren, P., Seong, Y.B., Oh, J.S., Rhee, H.H., Sandag, K., Yu, B.Y.: Late Quaternary glacial history of Khentey Mountains, Central Mongolia, Boreas, 48(3), 779-799, doi.org/10.1111/bor.12386, 2019.

Kirkbride, M., Winkler, S.: Correlation of Late Quaternary moraines: impact of climate variability, glacier response, and chronological resolution, Quat. Sci. Rev., 46, 1-29, https://doi.org/10.1016/j.quascirev.2012.04.002, 2012.

Klinge, M., Schneider, F., Dulamsuren, C., Arndt, K., Bayarsaikhan, U., & Sauer, D.: Interrelations between relief, vegetation, disturbances, and permafrost in the forest-steppe of central Mongolia. Earth Surf. Process. Landf., 46(9), 1766-1782, https://doi.org/10.1002/esp.5116, 2021

Kohl, C.P., Nishiizumi, K.: Chemical isolation of quartz for measurement of in situ -produced cosmogenic nuclides, Geochim. Cosmochim. Acta, 56(9), 3583-3587, https://doi.org/10.1016/0016-7037(92)90401-4, 1992.

Koppes, M., Gillespie, A.R., Burke, R.M., Thompson, S.C., Stone, J.: Late quaternary glaciation in the Kyrgyz Tien Shan. Quat. Sci. Rev., 27(7-8), 846-866, https://doi.org/10.1016/j.quascirev.2008.01.009, 2008.

Laabs, B. J., Licciardi, J. M., Leonard, E. M., Munroe, J. S., & Marchetti, D. W.: Updated cosmogenic chronologies of Pleistocene mountain glaciation in the western United States and associated paleoclimate inferences, Quat. Sci. Rev., 242, 106427, https://doi.org/10.1016/j.quascirev.2020.106427, 2020.

Laabs, B. J. C., & Munroe, J. S.: Late Pleistocene mountain glaciation in the Lake Bonneville basin, In Developments in Earth. Surf. Process., Vol. 20, pp. 462-503, https://doi.org/10.1016/B978-0-444-63590-7.00017-2, 2016

Laabs, B. J., Marchetti, D. W., Munroe, J. S., Refsnider, K. A., Gosse, J. C., Lips, E. W., ... & Singer, B. S.; Chronology of latest Pleistocene mountain glaciation in the western Wasatch Mountains, Utah, USA. Quaternary Research, 76(2), 272-284, https://doi.org/10.1016/j.yqres.2011.06.016, 2011

Laabs, B. J., Refsnider, K. A., Munroe, J. S., Mickelson, D. M., Applegate, P. J., Singer, B. S., & Caffee, M. W.: Latest Pleistocene glacial chronology of the Uinta Mountains: support for moisture-driven asynchrony of the last deglaciation, Quat. Sci. Rev., 28(13-14), 1171-1187, https://doi:10.1016/j.quascirev.2008.12.012, 2009.

Lee, M.K., Lee, Y.I., Lim, H.S., Lee, J.I., Yoon, H.I.: Late Pleistocene–Holocene records from Lake Ulaan, southern Mongolia: implications for east Asian palaeomonsoonal climate changes, J. Quat. Sci., 28(4), 370-378, https://doi.org/10.1002/jqs.2626, 2013.

Lehmkuhl, F., Grunert, J., Hülle, D., Batkhishig, O., Stauch, G.: Paleolakes in the Gobi region of southern Mongolia, Quat. Sci. Rev., 179, 1-23, https://doi.org/10.1016/j.quascirev.2017.10.035, 2018.

Li, Y., Liu, G., Chen, Y., Li, Y., Harbor, J., Stroeven, A.P., Caffee, M., Zhang, M., Li, C., Cui, Z.: Timing and extent of Quaternary glaciations in the Tianger Range, eastern Tian Shan, China, investigated using ^{10}Be surface exposure dating, Quat. Sci. Rev., 98, 7-23, https://doi.org/10.1016/j.quascirev.2014.05.009, 2014.

Licciardi, J. M., Clark, P. U., Brook, E. J., Elmore, D., & Sharma, P.: Variable responses of western US glaciers during the last deglaciation, Geology, 32(1), 81-84, https://doi.org/10.1130/G19868.1, 2004

Licciardi, J. M., Clark, P. U., Brook, E. J., Pierce, K. L., Kurz, M. D., Elmore, D., & Sharma, P.: Cosmogenic 3He and 10Be chronologies of the late Pinedale northern Yellowstone ice cap, Montana, USA, Geology, 29(12), 1095-1098, https://doi.org/10.1130/0091-7613(2001)029<1095:CHABCO>2.0.CO;2, 2001.

Licciardi, J. M., & Pierce, K. L.: History and dynamics of the Greater Yellowstone Glacial System during the last two glaciations, Quat. Sci. Rev., 200, 1-33, https://doi.org/10.1016/j.quascirev.2018.08.027, 2018

Lifton, N., Sato, T., Dunai, T.J.: Scaling in situ cosmogenic nuclide production rates using analytical approximations to atmospheric cosmic-ray fluxes, Earth Planet, Sci. Lett., 386, 149-160, https://doi.org/10.1016/j.epsl.2013.10.052, 2014.

Luckman, B. H.: The Geomorphic Activity of Snow Avalanches. Geografiska Annaler: Series A, Phys. Geogr., 59(1-2), 31-48, https://doi.org/10.1080/04353676.1977.11879945, 1977.

Meierding, T. C.: Late Pleistocene glacial equilibrium-line altitudes in the Colorado Front Range: a comparison of methods. Quat. Res., 18(3), 289-310. Research 18, 289-310, https://doi.org/10.1016/0033-5894(82)90076-X, 1982

Mischke, S., Lee, M.K., Lee, Y.I.: Climate history of southern Mongolia since 17 ka: The ostracod, gastropod and charophyte record from Lake Ulaan, Front, Earth Sci., 8, 221, https://doi.org/10.3389/feart.2020.00221, 2020.

NAMHEM.: Climate data. Institute for Hydrology and Aviation Meteorological Center of National Agency for Meteorology, Hydrology and Environmental Monitoring, Ulaanbaatar, Mongolia, 2020.

Nishiizumi, K., Imamura, M., Caffee, M., Southon, J., Finkel, R., McAninch, J.: Absolute calibration of ^{10}Be AMS Standards, Nucl. Instrum. Methods Phys. Res. B., 258(2), 403-413, https://doi.org/10.1016/j.nimb.2007.01.297, 2007.

National Oceanic and Atmospheric Administration.: US standard atmosphere (Vol. 76)., 1976

Oliva, M., Palacios, D., Fernández-Fernández, J. M., Rodríguez-Rodríguez, L., García-Ruiz, J. M., Andrés, N., ... & Hughes, P. D.: Late Quaternary glacial phases in the Iberian Peninsula, Earth-Sci, Rev., 192, 564-600, https://doi.org/10.1016/j.earscirev.2019.03.015, 2019.

Olson, M., & Rupper, S.: Impacts of topographic shading on direct solar radiation for valley glaciers in complex topography, The Cryosphere, 13(1), 29-40, 2019.

Palacios, D., Stokes, C. R., Phillips, F. M., Clague, J. J., Alcalá-Reygosa, J., Andrés, N., ... & Ward, D. J.: The deglaciation of the Americas during the Last Glacial Termination, Earth-Sci. Rev., 203, 103113, https://doi.org/10.1016/j.earscirev.2020.103113, 2020.

Porter, S.C.: Snowline depression in the tropics during the Last Glaciation. Quat. Sci. Rev., 20(10), pp.1067-1091, https://doi.org/10.1016/S0277-3791(00)00178-5, 2001

Pötsch, S.: Dynamics and paleo-climatic forcing of late Pleistocene glaciers in the Turgen and Khangai mountains (Mongolia) reconstructed from geomorphology, ^{10}Be surface exposure dating, and ice flow modelling. Ph.D. thesis, Greifswald, Finsterwalde, 2017.

Quirk, B. J., Moore, J. R., Laabs, B. J., Plummer, M. A., & Caffee, M. W.: Latest Pleistocene glacial and climate history of the Wasatch Range, Utah, Quat. Sci. Rev., 238, 106313, https://doi.org/10.1016/j.quascirev.2020.106313, 2020.

Ross, S.M.: Peirce's criterion for the elimination of suspect experimental data, J. Eng. Technol., 20(2), 38-41, 2003.

Rother, H., Lehmkuhl, F., Fink, D., Nottebaum, V.: Surface exposure dating reveals MIS-3 glacial maximum in the Khangai Mountains of Mongolia, Quat. Res., 82(2), 297-308, https://doi.org/10.1016/j.yqres.2014.04.006, 2014.

Sanders, J. W., Cuffey, K. M., Moore, J. R., MacGregor, K. R., & Kavanaugh, J. L.: Periglacial weathering and headwall erosion in cirque glacier bergschrunds. Geology, 40(9), 779-782, https://doi:10.1130/G33330.1, 2012

Şengör, A., Natal'In, B., Burtman, V.: Evolution of the Altaid tectonic collage and Palaeozoic crustal growth in Eurasia, Nature, 364(6435), 299-307, https://doi.org/10.1038/364299a0, 1993.

Seong, Y.B., Dorn, R.I., Yu, B.Y.: Evaluating the life expectancy of a desert pavement, Earth-Sci.Rev., 162, 129-154, https://doi.org/10.1016/j.earscirev.2016.08.005, 2016.

Shackleton, N.: Oxygen isotope analyses and Pleistocene temperatures re-assessed, Nature, 215(5096), 15-17, https://doi.org/10.1038/215015a0, 1967.

Shackleton, N.J.: The 100,000-year ice-age cycle identified and found to lag temperature, carbon dioxide, and orbital eccentricity, Science, 289(5486), 1897-1902, https://doi.org/10.1126/science.289.5486.1897, 2000.

Skinner, L., Shackleton, N.: An Atlantic lead over Pacific deep-water change across Termination I: implications for the application of the marine isotope stage stratigraphy, Quat. Sci. Rev., 24(5-6), 571-580, https://doi.org/10.1016/j.quascirev.2004.11.008, 2005.

Smith, S.G., Wegmann, K.W., Ancuta, L.D., Gosse, J.C., Hopkins, C.E.: Paleotopography and erosion rates in the central Hangay Dome, Mongolia: Landscape evolution since the mid-Miocene, J. Asian. Earth. Sci., 125, 37-57 DOI: https://doi.org/10.1016/j.jseaes.2016.05.013, 2016.

Tang, Z., & Fang, J.: Temperature variation along the northern and southern slopes of Mt. Taibai, China, Agric. For. Meteorol., 139(3-4), 200-207, https://doi.org/10.1016/j.agrformet.2006.07.001, 2006.

Tarasov, P., Peyron, O., Guiot, J., Brewer, S., Volkova, V., Bezusko, L., Dorofeyuk, N., Kvavadze, E., Osipova, I., and Panova, N.: Last Glacial Maximum climate of the former Soviet Union and Mongolia reconstructed from pollen and plant macrofossil data, Clim. Dyn., v. 15, no. 3, p. 227-240, https://doi.org/10.1007/s003820050278, 1999,

Thackray, G. D.: Varied climatic and topographic influences on Late Pleistocene mountain glaciation in the western United States, J. Quat. Sci.,: Published for the Quaternary Research Association, 23(6-7), 671-681, https://doi.org/10.1002/jqs.1210, 2008.

Thompson, W.G., Spiegelman, M.W., Goldstein, S.L., Speed, R.C.: An open-system model for U-series age determinations of fossil corals, Earth Planet. Sci. Lett., 210(1-2), 365-381, https://doi.org/10.1016/S0012-821X(03)00121-3, 2003.

Traynor, J., Sladen, C.: Tectonic and stratigraphic evolution of the Mongolian People's Republic and its influence on hydrocarbon geology and potential, Mar. Pet. Geol., 12(1), 35-52, https://doi.org/10.1016/0264-8172(95)90386-X, 1995.

Vassallo, R., Jolivet, M., Ritz, J.-F., Braucher, R., Larroque, C., Sue, C., Todbileg, M., Javkhlanbold, D.: Uplift age and rates of the Gurvan Bogd system (Gobi-Altay) by apatite fission track analysis, Earth Planet. Sci. Lett., 259(3-4), 333-346, https://doi.org/10.1016/j.epsl.2007.04.047, 2007.

Vassallo, R., Ritz, J.-F., Carretier, S.: Control of geomorphic processes on ^{10}Be concentrations in individual clasts: Complexity of the exposure history in Gobi-Altay range (Mongolia), Geomorphology, 135(1-2), 35-47, https://doi.org/10.1016/j.geomorph.2011.07.023, 2011.

Wang, Y.-J., Cheng, H., Edwards, R.L., An, Z., Wu, J., Shen, C.-C., Dorale, J.A.: A high-resolution absolute-dated late Pleistocene monsoon record from Hulu Cave, China, Science, 294(5550), 2345-2348, https://doi.org/10.1126/science.1064618, 2001.

Young, N. E., Briner, J. P., Leonard, E. M., Licciardi, J. M., & Lee, K.: Assessing climatic and nonclimatic forcing of Pinedale glaciation and deglaciation in the western United States, Geology, 39(2), 171-174, https://doi.org/10.1130/G31527.1, 2011.

Yu, K., Lehmkuhl, F., Diekmann, B., Zeeden, C., Nottebaum, V., Stauch, G.: Geochemical imprints of coupled paleoenvironmental and provenance change in the lacustrine sequence of Orog Nuur, Gobi Desert of Mongolia, J. Paleolimnol., 58(4), 511-532, https://doi.org/10.1007/s10933-017-0007-7, 2017.

Yu, K., Lehmkuhl, F., Schlütz, F., Diekmann, B., Mischke, S., Grunert, J., Murad, W., Nottebaum, V., Stauch, G., Zeeden, C.: Late Quaternary environments in the Gobi Desert of Mongolia: Vegetation, hydrological, and palaeoclimate evolution, Palaeogeogr. Palaeoclimatol. Palaeoecol., 514, 77-91, https://doi.org956/10.1016/j.palaeo.2018.10.004, 2019.

Zhang, S., Zhao, H., Sheng, Y., Chen, S., Li, G., & Chen, F.: Late Quaternary lake level record of Orog Nuur, southern Mongolia, revealed by optical dating of paleo-shorelines, Quat. Geochronol, 72, 101370, https://doi.org/10.1016/j.quageo.2022.101370, 2022.

LIST OF TABLES

LIST OF FIGURES

Table 1. Site parameters and glacier parameters used for the 2D ice surface model

Variable	Value	Unit
Time interval	22-16	ka
Day type	1 (calendar day)	
Day interval	152-243 (summer)	
Average elevation of site	3265.3	m
Modern summer temperature of Ikh Artsan	5.4	℃
Modern summer temperature of Jargalant	4.9	℃
LGM anomaly	-5.5	℃
Snow ratio (when temperature is below 0℃)	0.35	
Elevation of initial glacier’s toe (Ikh Artsan)	3385.1	m
Elevation of initial glacier’s toe (Jargalant)	3360.9	m
Elevation of the distal moraine (Ikh Artsan)	3222.2	m
Elevation of the distal moraine (Jargalant)	2997.2	m
Headwall altitude (Ikh Artsan)	3508.3	m
Headwall altitude (Jargalant)	3533.3	m
Glacial bed shear stress (Ikh Artsan)	100	kPa
Glacial bed shear stress (Jargalant)	200	kPa

Table 2. Key parameters of glacial mass balance model

	Variable	Optimized values/Unit		Variable	Optimized values/Unit
	Mass balance calculation (m, mm)			**Air pressure calculation (P_h, Pa)**	
c	Accumulation	mm, m	P_0	Pressure at reference point (sea level)	1013.25 Pa
a	Ablation/melt	mm, m	T_h	Air temperature at the height h	Pa
	Melt calculation (a, m)		T_0	Air temperature at the reference point	288.15 K
n	Number of time steps per day		M	Mass per air molecule	0.0290 kg mol^{-1}
MF	Melt factor	1.8 mm d^{-1} °C^{-1}	g	Acceleration due to gravity	9.8067 m s^{-2}
a_{ice}	Radiation coefficient for ice surfaces	0.0008	R	Universal gas constant	8.3143 mol K
I	Potential clear-sky direct solar radiation at the glacier	W m-^{2}	L	Atmospheric lapse rate	-0.008 K m-^{1}
T	Monthly air temperature	℃		**Zenith angle calculation (Z, °) and angle of incidence (θ, °)**	
	Insolation calculation (I, w m^{-2})		δ	Solar declination angle	°/Radian
I_0	Solar constant	1367 W m^{-2}	φ	Latitude	°/Radian
R_m/R	Eccentricity correction factor of the earth's orbit		ω	Hour angle	°/Radian
Ψ_a	Atmospheric transmissivity	0.75	β	Slope inclination angle	°/Radian
P_h	Air pressure at the height	Pa	γ	Surface azimuth angle	°/Radian
P_0	Air pressure at reference point (sea level)	1013.25 Pa			
Z	Zenith angle	°			
θ	Angle of incidence	°			

Table 3. LGM ELA reconstruction

Sites	Top of the rock cliff (m a.s.l)	Altitude of cirque floor (m a.s.l)	Headwall altitude [a] (m a.s.l)	Toe altitude, LGM (m a.s.l)	THAR ELA [b] (m a.s.l)
Jargalant valley	3620	3360	3533	2997	3308
Ikh Artsan valley	3560	3385	3508	3222	3388
Average					3348

[a] Headwall altitude for LGM glaciers was selected at one-third of the altitude difference between the top of the rock cliff and the cirque floor (Goldthwait, 1970).

[b] THAR of 0.58 was used for calculating LGM ELA (Batbaatar et al., 2018). ALOS PALSAR DEM with spatial resolution of 12.5 m is used to extract corresponding elevations. Altimetric error (vertical uncertainty) is ~5-7 m (Chai et al., 2022, Ferreira and Cabral, 2022).

Table 4. Result of ^{10}Be exposure age dating

Moraine group	Name	Latitude (˚N, DD)	Longitude (˚E, DD)	Elevation (m a.s.l)	Thickness [a] (cm)	Shielding factor [b]	Quartz [c] (g)	Be carrier [d] (g)	$^{10}Be/^{9}Be$ [e, f] (10^{-13})	^{10}Be conc.[d, f] (10^5 atoms g^{-1})	Exposure age [f, g, i] (ka) LSDn
M_{IA1}	IAM001	44.95421	100.2602	3289	2	0.7746	20.3	0.3729	6.0 ± 0.2	7.7 ± 0.3	19.9 ± 1.4
	IAM002	44.95429	100.26022	3290	2.5	0.7746	17.52	0.3796	5.3 ± 0.2	8.0 ± 0.3	20.7 ± 1.4
	IAM003	44.95427	100.2603	3289	3.5	0.7746	20	0.3849	6.1 ± 0.2	8.1 ± 0.3	21.2 ± 1.5
	IAM004	44.95438	100.26035	3289	3.5	0.7746	14.69	0.3958	4.1 ± 0.1	7.6 ± 0.3	19.9 ± 1.4
	IAM005	44.95435	100.26015	3290	3	0.7746	19.75	0.3704	5.7 ± 0.2	7.4 ± 0.2	19.3 ± 1.3
	IAM006	44.95437	100.26006	3288	3.5	0.7746	19.54	0.3812	5.7 ± 0.2	7.7 ± 0.2	20.3 ± 1.4
	IAM007	44.95438	100.26004	3288	4	0.7746	18.96	0.3738	5.3 ± 0.2	7.2 ± 0.2	19.1 ± 1.3
M_{J4}	JAM001	44.97614	100.29007	3412	3	0.8218	16.91	0.3842	78.6 ± 0.6	124.9 ± 1.6	278.9 ± 18.1
	JAM002	44.97627	100.29012	3411	4	0.8218	20	0.3993	57.0 ± 0.6	79.7 ± 1.1	177.3 ± 11.3
	JAM003	44.97651	100.29021	3411	2.5	0.8218	20.03	0.3871	194.3 ± 1.2	262.9 ± 3.1	636.2 ± 45.1
	JAM004	44.97654	100.28988	3409	3	0.8218	20	0.382	70.9 ± 0.6	94.8 ± 1.3	208.9 ± 13.3
	JAM005	44.97665	100.29008	3409	2.5	0.8218	20.03	0.375	64.8 ± 0.5	84.9 ± 1.1	186.6 ± 11.8
M_{J3}	JAM006	44.97891	100.29092	3350	3	0.8363	20.02	0.3708	12.3 ± 2.6	15.9 ± 3.4	35.9 ± 8.0
	JAM007	44.97886	100.29079	3351	3	0.8363	20.03	0.3707	25.3 ± 5.0	32.8 ± 6.5	74.1 ± 15.7
	JAM008	44.97894	100.29084	3350	3	0.8363	20.42	0.3932	68.9 ± 7.0	92.9 ± 9.5	209.0 ± 26.1
	JAM009	44.97891	100.29095	3348	3.5	0.8363	19.97	0.3832	15.3 ± 2.7	20.5 ± 3.7	45.8 ± 8.7
	JAM010	44.97897	100.29089	3348	3.5	0.8363	19.97	0.3856	40.9 ± 5.7	55.2 ± 7.7	123.8 ± 19.4
M_{J2}	JAM011	44.98058	100.29328	3293	2.5	0.8598	19.91	0.3903	52.3 ± 0.5	71.7 ± 1.0	162.1 ± 10.2
	JAM012	44.98083	100.29321	3289	2	0.8598	19.97	0.3785	93.6 ± 0.6	124.2 ± 1.5	284.9 ± 18.4
	JAM013	44.98095	100.29263	3289	4	0.8598	20.22	0.3794	81.0 ± 4.1	106.4 ± 5.5	246.6 ± 20.6
	JAM014	44.98096	100.29259	3292	3	0.8598	20.38	0.3812	61.0 ± 6.4	79.9 ± 8.4	181.9 ± 23.0
	JAM015	44.98096	100.2926	3292	3	0.8598	20.04	0.3894	59.4 ± 5.2	80.8 ± 7.1	184.0 ± 20.3
M_{J1}	JAM016	44.98224	100.29684	3193	3.5	0.8852	19.91	0.3872	3.0 ± 0.1	4.0 ± 0.2	10.6 ± 0.8
	JAM017	44.98232	100.29693	3191	3	0.8852	20.05	0.3935	4.8 ± 0.3	6.6 ± 0.4	16.3 ± 1.4
	JAM018	44.98232	100.29693	3191	2.5	0.8852	20.06	0.3864	5.8 ± 0.4	7.8 ± 0.5	18.9 ± 1.7
	JAM019	44.98326	100.29745	3170	3	0.8935	20.17	0.3962	4.4 ± 0.2	6.0 ± 0.3	15.1 ± 1.3
	JAM020	44.98379	100.29716	3172	3.5	0.9311	20.14	0.3865	5.8 ± 0.2	7.7 ± 0.2	18.2 ± 1.2
	JAM021	44.98385	100.29712	3171	3	0.9311	20.04	0.3879	5.4 ± 0.2	7.3 ± 0.2	17.4 ± 1.2

[a] Sampling thickness of the boulders' outermost exposed surfaces.
[b] Topographic shielding factors for each sampling site were measured at intervals of 30°.
[c] Weight of the pure quartz. The density of granite (2.7 g cm^{-3}) was used to calculate exposure age.
[d] A mean value of process blank samples ($4.53 \times 10^{-15} \pm 1.62 \times 10^{-15}$) was used for correction.

[e] Ratios of $^{10}Be/^{9}Be$ were normalized with 07KNSTD reference sample 5-1 prepared by Nishiizumi et al. (2007) with a $^{10}Be/^{9}Be$ ratio of $2.71\times10^{-11} \pm 4.71\times10^{-13}$ (calibrated error) and using a ^{10}Be half-life of 1.36×10^{6} years (Chmeleff et al., 2010; Korschinek et al., 2010)
[f] Uncertainties were calculated at the 1σ confidence level.
[g] Exposure ages, assuming zero erosion were calculated using CRONUS-Earth online calculator version 3.0.2 (Balco et al., 2008).
[h] Constant production rate of the ^{10}Be model of Stone (2000) was used for calculating exposure age.
[i] Constant production rate of the ^{10}Be model of Lifton et al. (2014) was used.

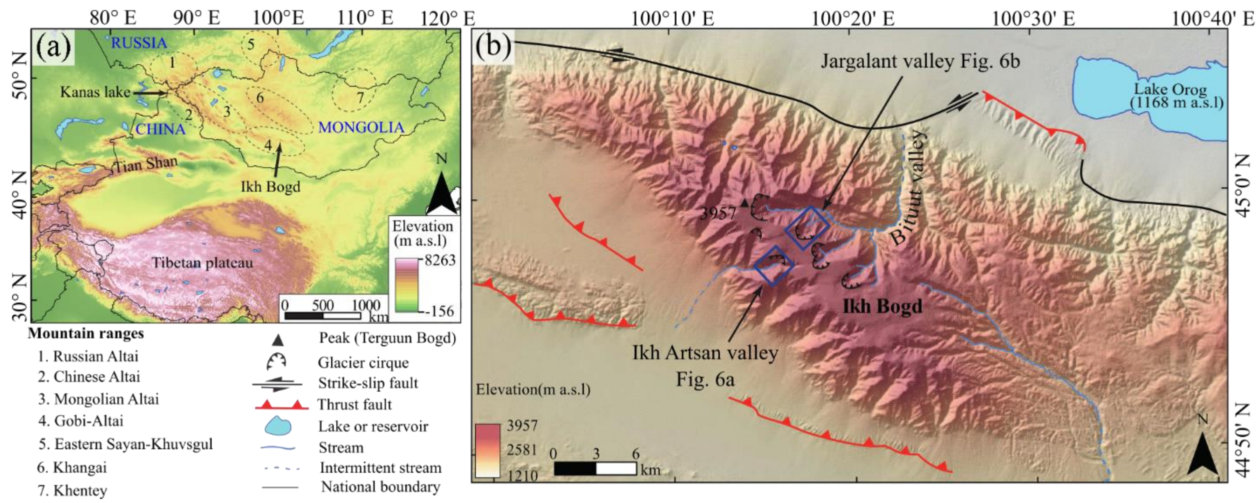

Fig. 1. Study area. (a) Central Asian glaciated mountain ranges during late Quaternary. (b) Study area. Boxed areas indicate Ikh Artsan and Jargalant valleys. See the detailed maps of both valleys visualized in Figs. 4-6. The background image is shaded SRTM DEM with 30 m resolution.

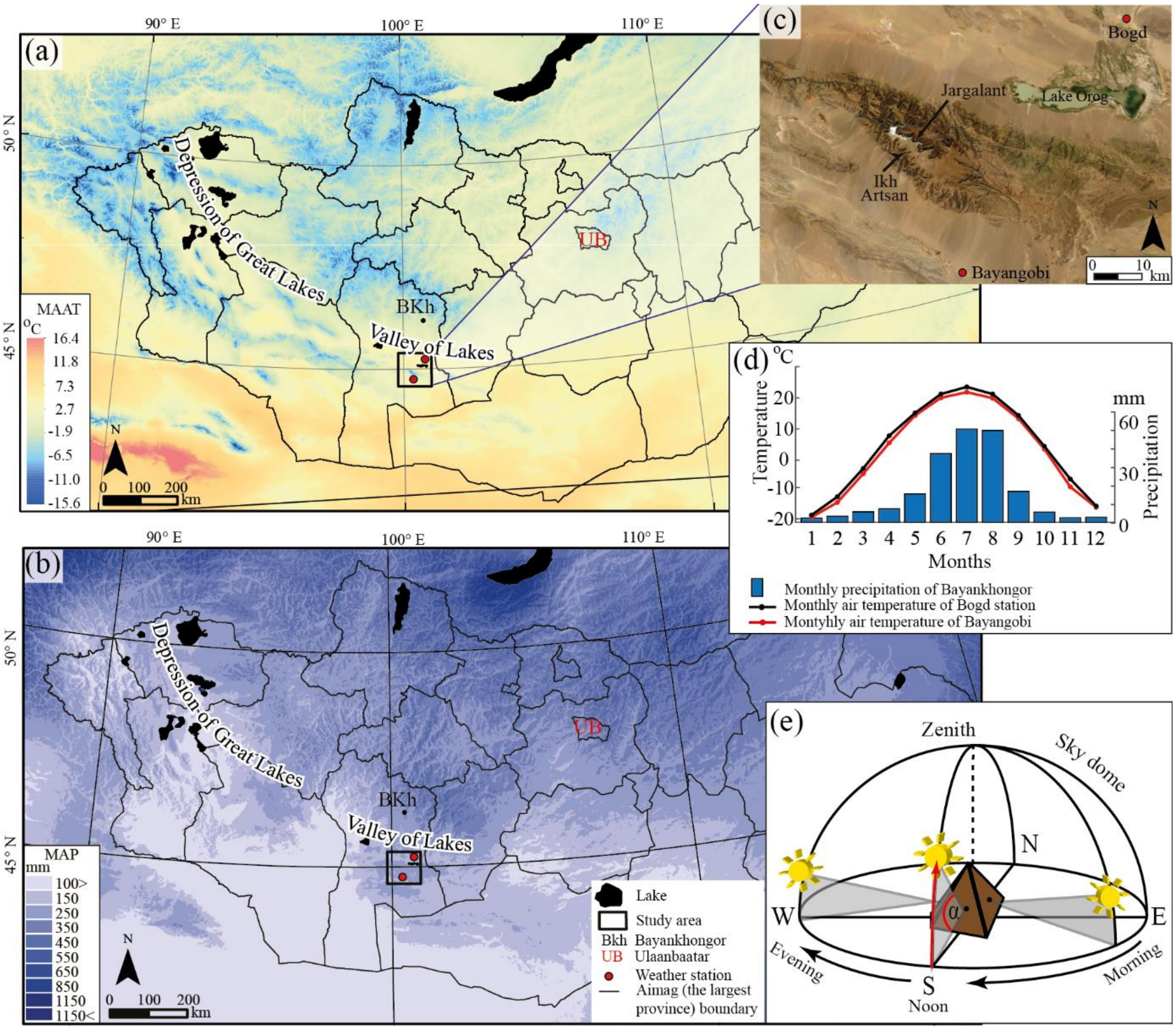

Fig. 2. The present-day climate of Mongolia. (a) Mean annual air temperature across Mongolia. (b) Mongolian mean annual precipitation. BKh (black dot) represents Bayankhongor aimag (the largest unit of province) center, and UB is Ulaanbaatar, the capital of Mongolia. Red dots mark the nearest weather stations to the study area. Temperature data (CHELSA_Bio10_01, at 30 arc-second) and precipitation data (CHELSA_Bio10_12, at 30 arc-second) are long-term (1973-2013) annual means. Source: Bioclim Bio1 data, CHELSA V 1.2 (Karger et al., 2017). (c) The exact locations of the nearest weather stations to the massif, Bayangobi (1540 m a.s.l) and Bogd (1240 m a.s.l). (d) Long-term (1989-2019) monthly mean temperature from Bogd station (black graph) and Bayangobi station (red graph). Monthly mean precipitation (2005-2019) of Bayankhongor is described as blue bar chart (NAMHEM, 2020). (e) Solar altitude angles on the mountain slopes with different aspect. Solar altitude angles (α) at different hour angles (morning to evening). Solar altitude angle is 0 degree at sunrise and reaches its maximum value at noon. In the mountainous area of northern hemisphere, south-facing slope receives highest energy at noon, however, north-facing slope receives less or no energy due to topographic shading effect.

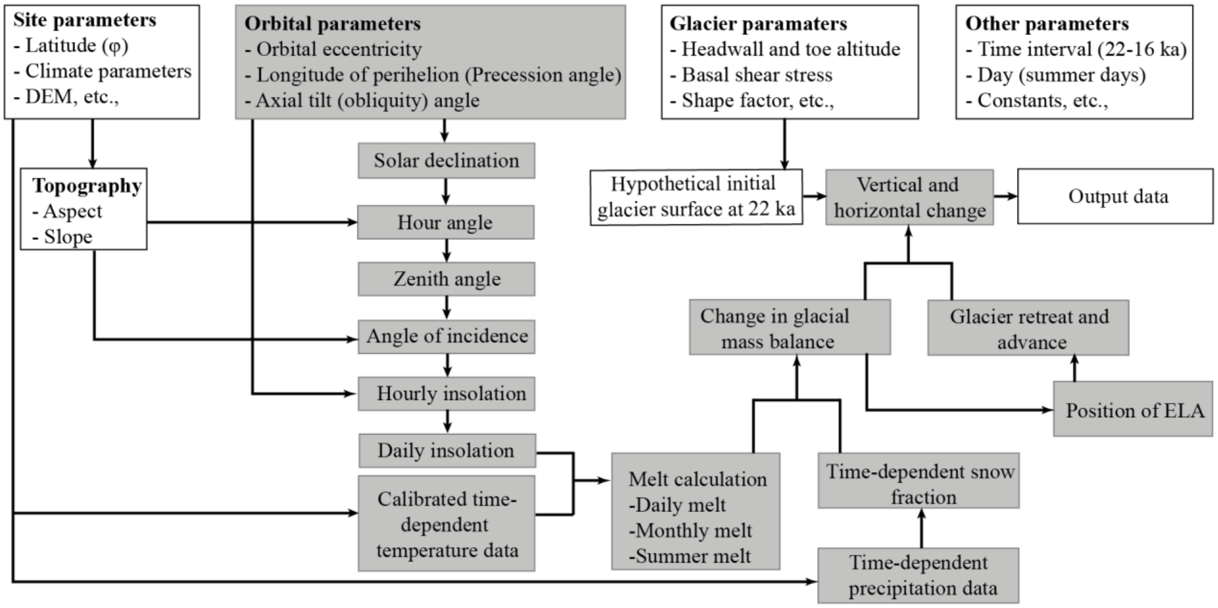

Fig. 3. Source code structure diagram of 2D ice surface modelling

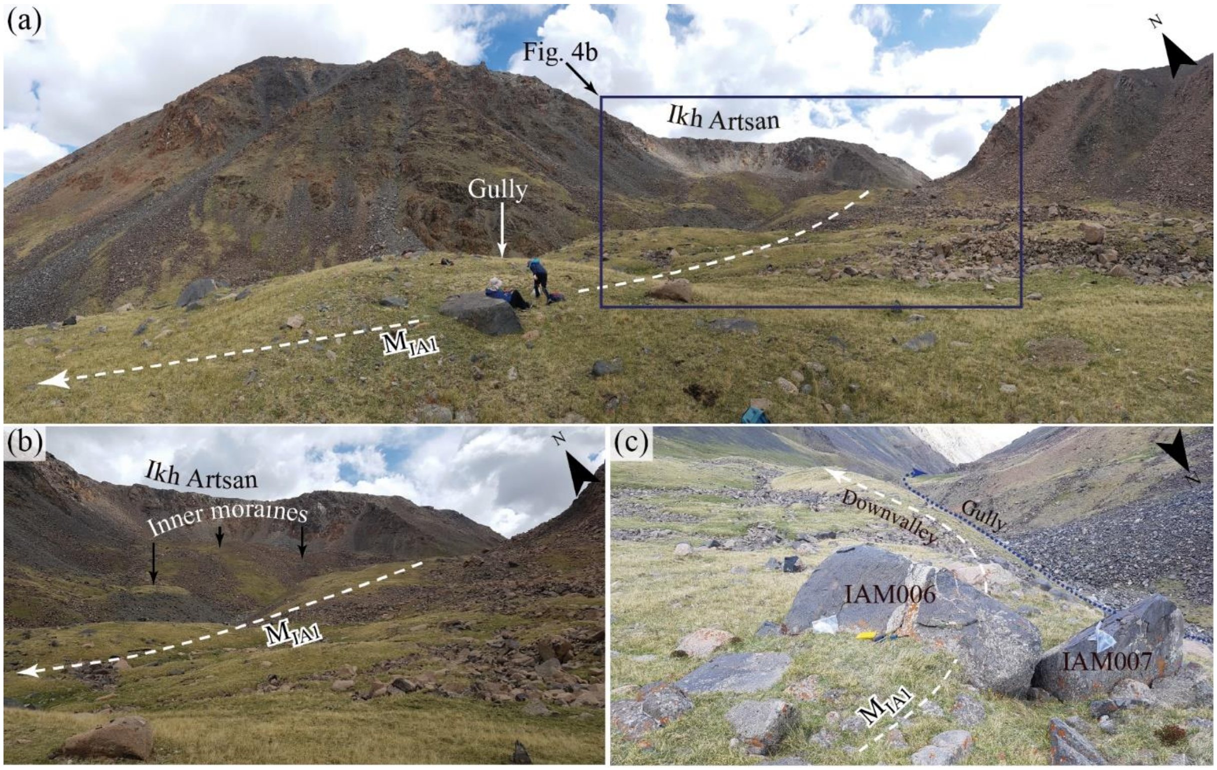

Fig. 4. Photo composites of the Ikh Artsan valley and paleoglacial evidence. (a) Ikh Artsan glacial cirque and distal moraine ridge. The white dashed arrow represents M_{IA1} moraine ridge, which marks the farthest extent of late Quaternary glaciation. (b) Distal and inner moraine sequences (Batbaatar et al., 2018). (c) IAM006 and IAM007 sampling boulders are on the M_{IA1} moraine ridge.

Fig. 5. Geomorphologic setting and moraine stratigraphy in Jargalant valley. (a) Jargalant valley and Bituut trunk valley that extends from the cirque near the highest peak (3957 m a.s.l). Jargalant valley is one of the large tributaries of Bituut valley, while covered by a large amount of late Quaternary moraine complex. (b) The stratigraphic boundary between M_{J4} and M_{J3} moraines in the Jargalant cirque. Moraines are dissected by longitudinal gullies. (c) Pair of M_{J2} moraine and oldest M_{J1} moraine ridge. Horses (red circle) are for scale. (d) Boulder sizes on M_{J2} moraine range from sub-meter to several meters. (e) Downvalley view of the moraine sequences from the uppermost moraine sequence.

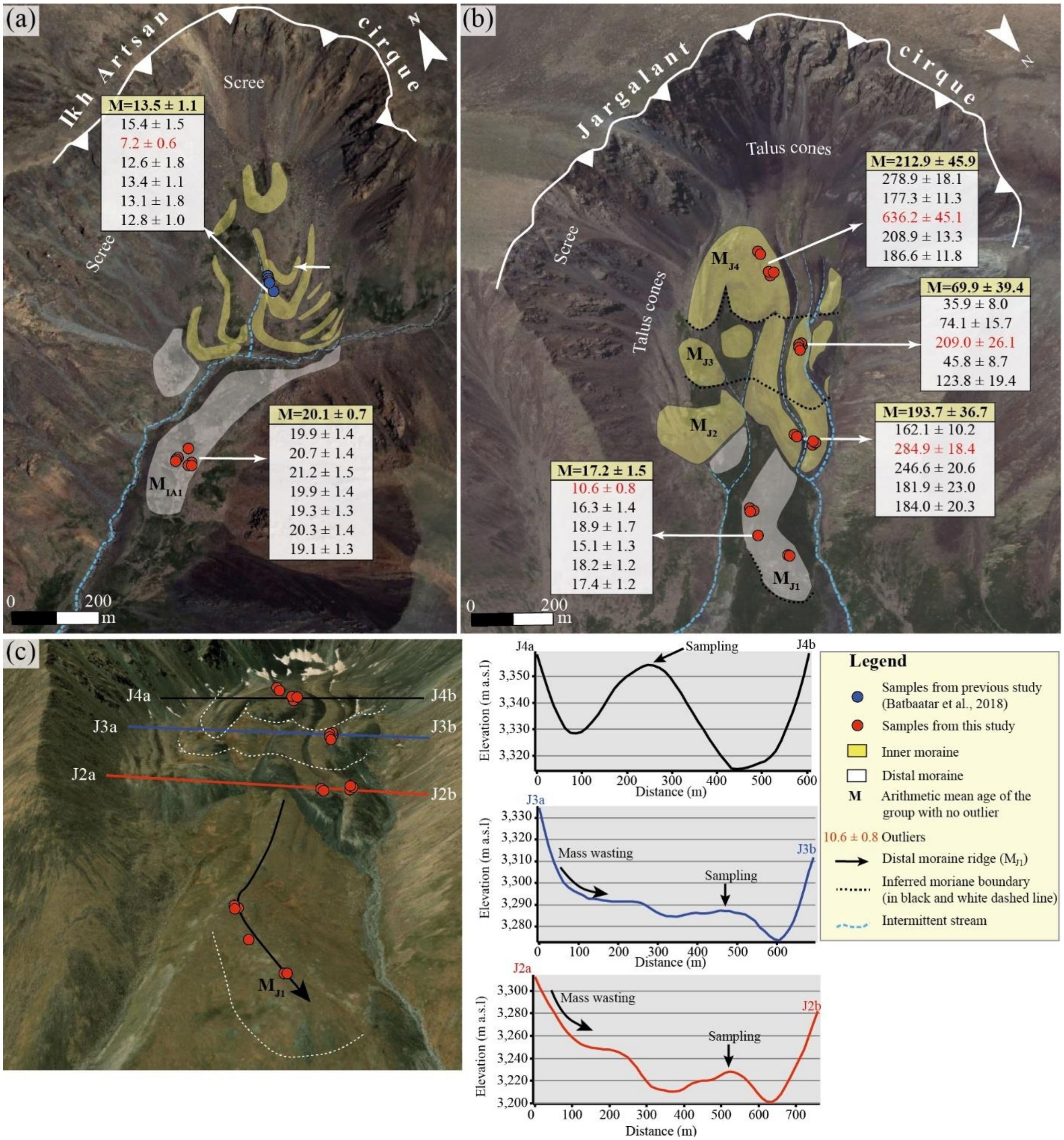

Fig. 6. ^{10}Be Exposure ages (ka) for outer (white) and inner (yellow) moraine sequences. (a) Exposure ages from Ikh Artsan moraine sequences. (b) Age dating result of Jargalant hummocky moraine complex. Background images of (a) and (b) are Bing Maps © Microsoft (2023) aerial imageries. (c) Cross-section view of inner moraine sequences (M_{J4} ~ M_{J2}) of Jargalant valley. Background image is oblique imagery of © ArcGIS Earth (2023) V1.16.0.3547. Mass wasting deposits on the moraine surface and intermittent stream incision have altered the original moraine morphologies. Samples were taken from the highest intact point of the longitudinally elongated moraine ridge, which thought to be unaffected by reworking processes. Since the exposure age dating result from inferred inner moraine sequences (M_{J4} ~ M_{J2}) shows high inheritance, which cannot contribute the inferred moraine sequences.

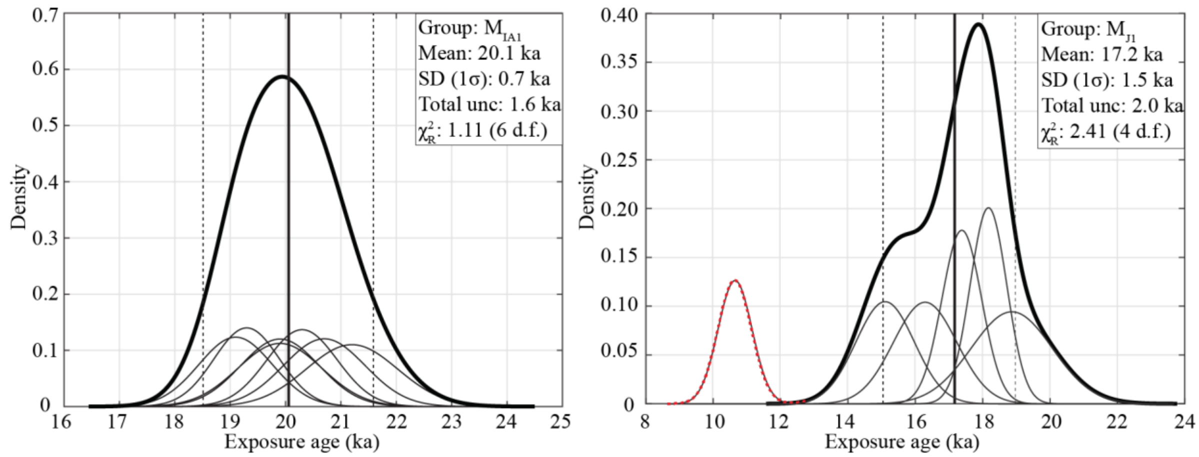

Fig. 7. Kernel density plot (KDP) of estimated [10]Be exposure ages from distal moraine crests in Jargalant and Ikh Artsan valleys. Plots were created using IceTEA Matlab code by Jones et al. (2019). (a) KDP of exposure ages of the most extensive moraine sequence (M_{IA1}) in Ikh Artsan valley. No outlier was detected. The arithmetic mean was calculated and marked as a bold solid vertical line. (b) KDP of exposure ages from the oldest (M_{J1}) moraine sequence in Jargalant valley. The outlier was excluded by Chauvenet, Pierce, and the standardized deviation method in the 1 sigma range. The thick solid lines represent the cumulative density curve, the dashed red line shows excluded outlier, and solid, narrow black lines show individual density curves for each sample. The range of total uncertainty of the group is marked as two vertical dashed lines. The sample statistics were calculated after rejecting outliers, while internal errors were used to create KDP and calculate sample statistics.

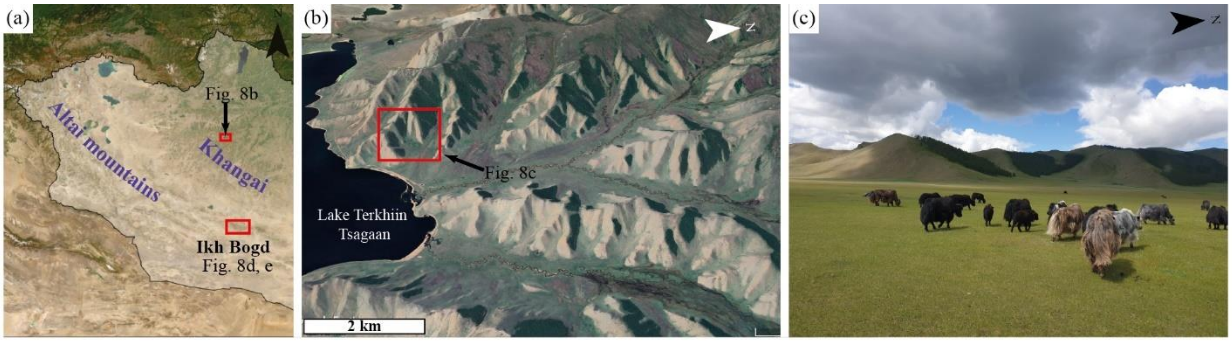

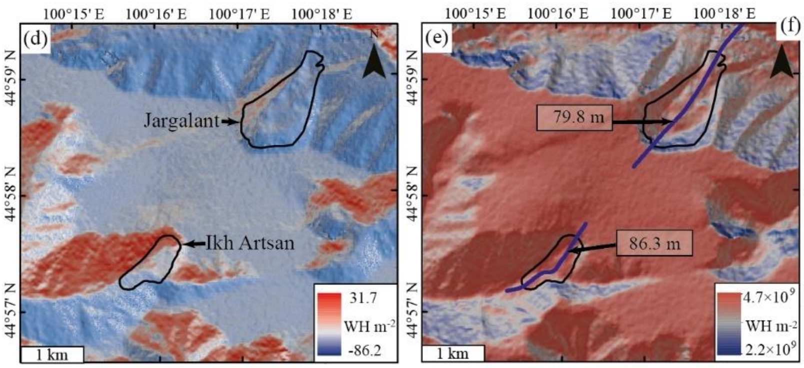

(f)

Time interval (ka)	Total melt (m) Ikh Artsan	Total melt (m) Jargalant	Melt excess (m)
22-21	0.6	0	0.6
21-20	3.7	0	3.7
20-19	14.0	0.2	13.8
19-18	15.9	0.5	15.4
18-17	22.5	4.3	18.1
17-16	31.2	11.5	19.7
22-16	86.3	16.2	70
Jun 21, 22 ka	0.0 mm	0 mm	0 mm
Jun 21, 20 ka	3.7 mm	0 mm	3.7 mm
Jun 21 present-day	47.0 mm	40.5 mm	6.6 mm

Fig. 8. Asymmetric distribution of potential clear-sky direct solar radiation, glacial melt, and vegetation on the south- and north-facing slopes. (a) Location map of Ikh Bogd and lake Terkhiin Tsagaan. (b, c) Tree distribution on north-facing slope, north of lake Terkhiin Tsagaan (© Google Earth 2022; photo taken by authors). (d) Anomaly of total clear-sky direct solar radiation of June solstice in 20 ka from modern value. (e) Integrated total summer insolation for 22-16 ka. The purple line represents profile along midline in Ikh Artsan and Jargalant valley. Integrated total melt was calculated in Ikh Artsan as 86.3 m and 79.8 m in Ikh Artsan valley for 22-26 ka at the same temperature. (f) Integrated total melt calculation for Ikh Artsan and Jargalant valley considering average summer temperature in Jargalant is 0.5 lower than that in Ikh Artsan.

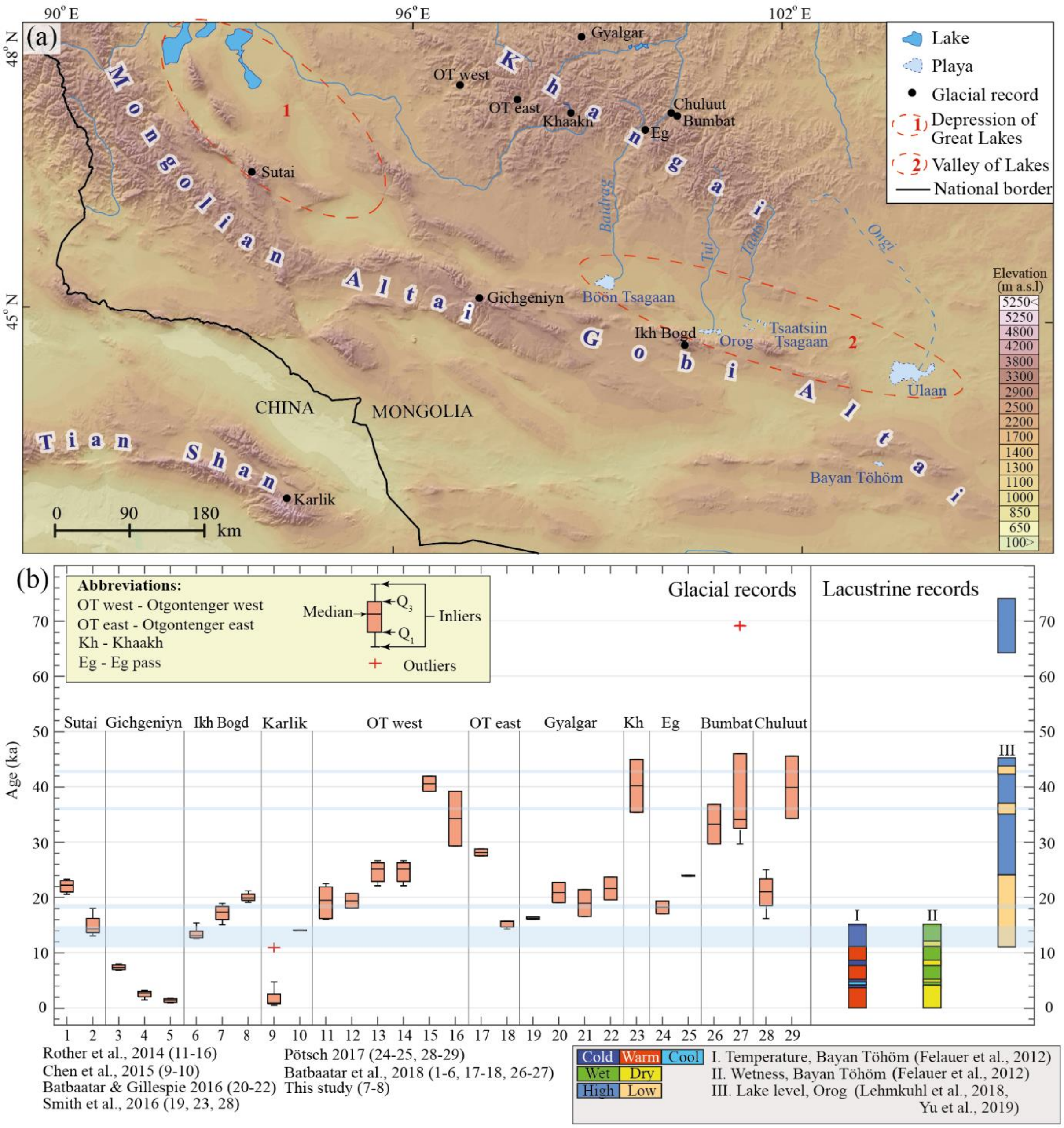

Fig. 9. Temporal and spatial distributions of glacial and paleo-lacustrine records in the neighboring regions of Ikh Bogd massif. (a) Locations of the ^{10}Be age dating sites for paleoglaciers and paleo lacustrine proxies. (b) Age dating results from glaciers and lacustrine proxies. Glacial records on the left are the ^{10}Be exposure age dating results representing 29 individual moraine groups. Exposure ages were recalculated with Cronus Earth V3, using the LSDn scaling factor (Lifton et al., 2014). Only effective ages were plotted after outlier rejection using the Chauvenet, Peirce, and normalized deviation method. On each box, central mark indicates the median, and the bottom and top edges of the box indicate the 25th (Q_1) and 75th (Q_3) percentiles, respectively. The whiskers extend only to the data points considered inliers, and the additional outliers were detected from the effective ages and plotted individually using the '+' marker symbol. The shaded light blue sections on the age interval present the major harsh periods (playa phase of Orog, Yu et al., 2019). Lacustrine records on the right present temperature (I) and wetness data (II) in lake Bayan Töhöm and lake level record of lake Orog (III).

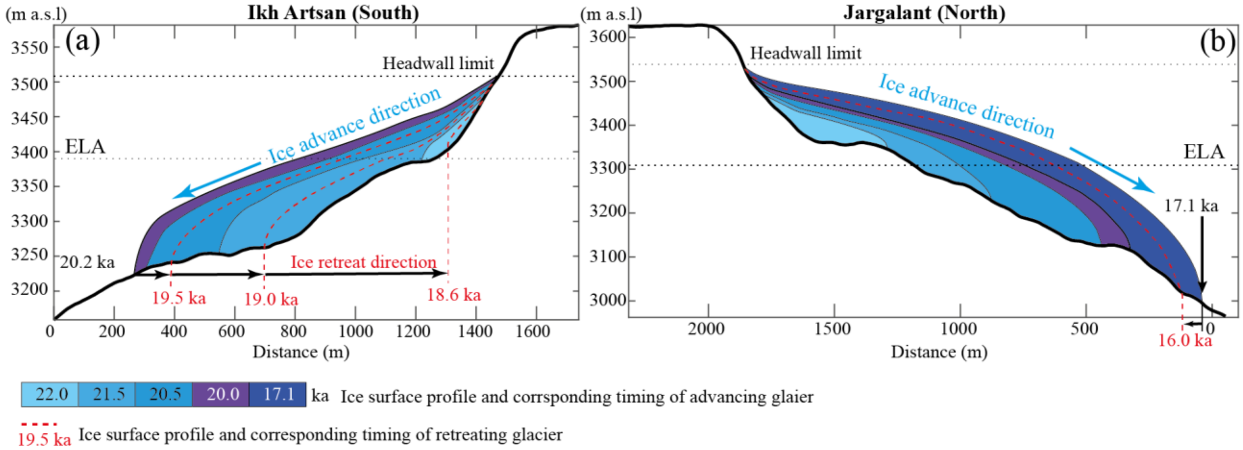

Fig. 10. Asynchronous advance and retreat pattern of Ikh Bogd paleoglacier during 22-16 ka. (a) Paleoglacier in Ikh Artsan valley advanced between 22.0 and 20.2 ka and retreated from 20.2 to 18.6 ka. (b) Paleoglacier in Jargalant valley most expanded downvalley between 22.0 and 17.1 ka. Small retreat is observed during 17.1-16.0 ka. The present-day summer temperature in the north-facing valley was considered 0.5 °C lower than in the south-facing valley. The present-day temperature is calibrated to Greenland (NGRIP) paleotemperature data (Buizert et al., 2018) using an LGM summer temperature anomaly of -5.5 °C. Headwall altitudes of the LGM paleoglaciers were used to mark the maximum thickness of the glacier.

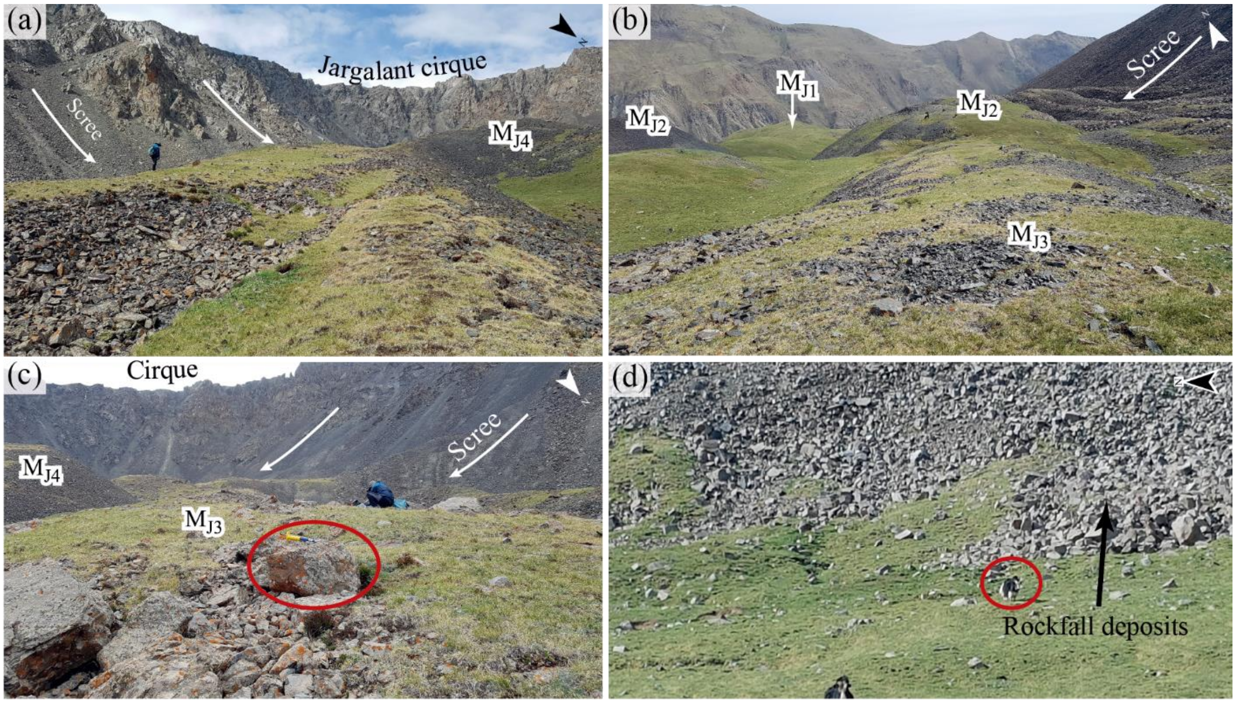

Fig. 11. Rockfall deposits in Jargalant valley. The scree or talus cone was on the cirque wall. M_{J4}, M_{J3}, and M_{J2} moraine formed within a Jargalant cirque, consequently outer edges of moraine ridges near the cirque wall were covered with talus deposit. (a) Rockfall deposit on the southeastern cirque wall, near M_{J4} moraine. (b) Scree covering on M_{J2} moraine that is dissected by an intermittent stream. (c) Sampling site of M_{J3} moraine and scree on the southern and southwestern wall of the cirque, near M_{J4}, M_{J3} moraine. JAM010 was taken from the circled boulder. Chisel, for scale, is on the boulder. (d) Rockfall deposit on the eastern slope of the cirque. Yak (circled) is for scale.

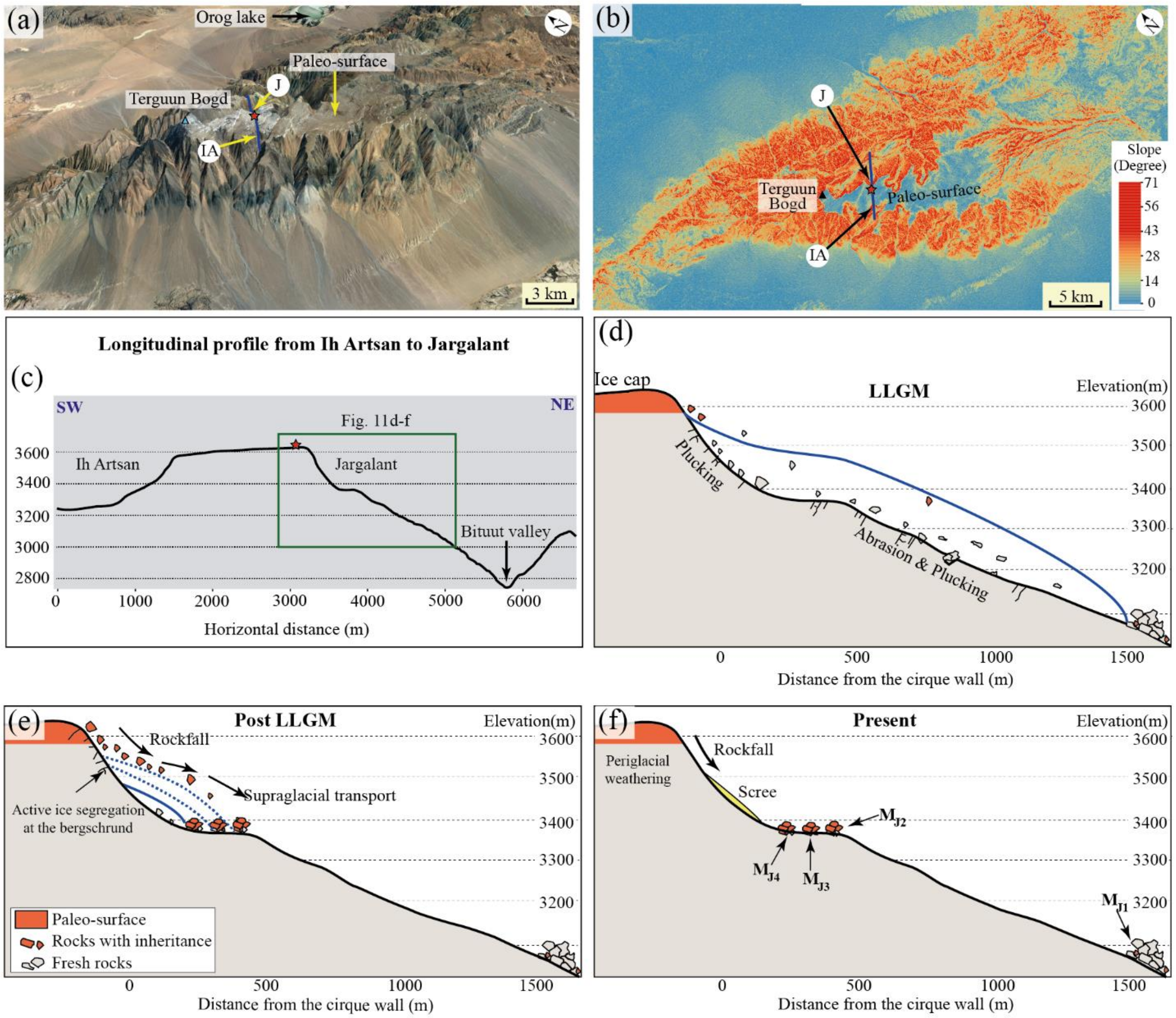

Fig. 12. Inheritance from the uplifted paleo-surface of Ikh Bogd massif. (a) 3D view of the paleo-planation surface (© Google Earth, 2022). (b) Slope map of Ikh Bogd, location of the Ikh Artsan (IA) and Jargalant (J) valley. The green triangle represents the highest peak of the massif, Terguun Bogd. Exposure age and erosion rate (Table 2) were calculated using the highest concentration of the boulder from M_{J4}-M_{J2} (Fig. 11a) for the point location marked as red star (Fig. 11b; 3625 m). (c) Longitudinal profile along a dark blue line (See Fig. 11b) connecting Ikh Artsan and Jargalant valley from SW to NE. (d) LLGM (Local LGM ~17 ka) glacial extent. Plucking of fresh rocks was intensive due to glacial length and thickness. (e) Enhanced supply of highly inherited rocks into M_{J4}, M_{J3}, and M_{J2} moraine series which are formed by successive glacial advances or/and stagnation. According to a shortage of glacier length, low number of fresh rocks are plucked out. Thinned glacier allows intensive ice segregation along the bergschrund and more inherited rockfalls into the ice surface. Hence, boulder supply with inheritance of paleo surface would increase. (f) Present-day rockfall deposit without supraglacial transport.